J. Fluid Mech. (2012), *vol.* 697, *pp.* 336–366. © Cambridge University Press 2012
doi:10.1017/jfm.2012.69

Boundary layers and wind in cylindrical Rayleigh–Bénard cells

Sebastian Wagner†, Olga Shishkina and Claus Wagner

German Aerospace Center (DLR), Institute of Aerodynamics and Flow Technology, Bunsenstrasse 10, 37073 Göttingen, Germany

(Received 4 November 2011; revised 30 January 2012; accepted 1 February 2012; first published online 6 March 2012)

We analyse the wind and boundary layer properties of turbulent Rayleigh–Bénard convection in a cylindrical container with aspect ratio one for Prandtl number $Pr = 0.786$ and Rayleigh numbers (Ra) up to 10^9 by means of highly resolved direct numerical simulations. We identify time periods in which the orientation of the large-scale circulation (LSC) is nearly constant in order to perform a statistical analysis of the LSC. The analysis is then reduced to two dimensions by considering only the plane of the LSC. Within this plane the LSC is treated as a wind with thermal and viscous boundary layers developing close to the horizontal plates. Special focus is on the spatial development of the wind magnitude and the boundary layer thicknesses along the bottom plate. A method for the local analysis of the instantaneous boundary layer thicknesses is introduced which shows a dramatically changing wind magnitude along the wind path. Furthermore a linear increase of the viscous and thermal boundary layer thickness along the wind direction is observed for all Ra considered while their ratio is spatially constant but depends weakly on Ra. A possible explanation is a strong spatial variation of the wind magnitude and fluctuations in the boundary layer region.

Key words: boundary layer structure, Bénard convection, turbulent convection

1. Introduction

One of the classical problems in fluid dynamics is the flow driven by the temperature difference between a heated bottom and a cooled top plate. This is a simplified model for many convective flow phenomena occurring on the Earth, e.g. in the atmosphere, as well as extraterrestrial such as the convection in stars. Named after its first two investigators, Rayleigh–Bénard convection (RBC) has been studied for more than hundred years. Nevertheless it is still under extensive investigation, since many aspects are not yet well understood.

Over recent decades the scaling of two important system responses, the Nusselt number Nu and the Reynolds number Re, with the governing dimensionless parameters, the Rayleigh number Ra and the Prandtl number Pr, has been studied theoretically, experimentally and numerically. For recent reviews we refer to Ahlers, Grossmann & Lohse (2009*b*) and Lohse & Xia (2010).

The flow typically found in Rayleigh–Bénard cells with aspect ratios (diameter/height) of order unity is characterized by the boundary layers (BLs) close

† Email address for correspondence: Sebastian.Wagner@DLR.de

https://doi.org/10.1017/jfm.2012.69 Published online by Cambridge University Press

to the rigid walls and the large-scale flow motion. Their interaction is a key point in understanding the system's responses to the temperature difference and is the subject of several theoretical studies, among which Kraichnan (1962), Castaing *et al.* (1989), Shraiman & Siggia (1990), Grossmann & Lohse (2000) and Hölling & Herwig (2006) should be mentioned here. The theoretical models developed are in most cases based upon assumptions on the structure of the BLs and their interaction with the bulk region.

Besides checking whether the theories give accurate predictions of the convection system's responses it is also necessary to verify the assumptions they are based on. In the Grossmann–Lohse (GL) theory the BLs are assumed to be of Prandtl–Blasius (PB) type (Grossmann & Lohse 2011) (up to a shear Reynolds number of $Re_s \approx 420$). Prandtl–Blasius BL theory (Schlichting & Gersten 2006) is a successful approach to approximate the BLs occurring when a laminar and stationary wind of constant magnitude flows over a flat plate of semi-infinite length and infinite width. It not only gives an analytical solution (within a set of approximations) for the BL profile but also for the development of its width and other characteristics along the plate. In a confined Rayleigh–Bénard cell the situation is very different from a semi-infinite plate and a constant wind velocity. This might have a negligible influence on the mean heat flux (Nusselt number) scaling with the Rayleigh number, but can lead to deviations of other local quantities from the PB predictions.

The usual check for whether PB BLs occur is through the analysis of the time- and spatially averaged vertical profiles of temperature and velocity (Tilgner, Belmonte & Libchaber 1993; Hölling & Herwig 2006; Sun, Cheung & Xia 2008; du Puits, Resagk & Thess 2009; Shishkina & Thess 2009; Stevens, Verzicco & Lohse 2010). In some cases strong deviations from PB profiles are found. This is partially explained by recent studies of Zhou & Xia (2010) and Zhou *et al.* (2010) which show that an instantaneous analysis and a more complex rescaling lead to better agreement. These studies are focused on profiles averaged spatially over a small region around the vertical centreline of the cell, which make it impossible to compare them with predictions of the PB theory on the spatial development of certain BL characteristics like its thickness along the wind direction. In a recent paper by Zhou *et al.* (2011), in which the horizontal dependence of BL profiles is investigated by means of two-dimensional numerical simulations, it was found that the BL thickness develops in a complicated way along the wind direction. In the present paper we develop a method to analyse the spatial behaviour of instantaneous as well as time-averaged local profiles and BL characteristics.

To ensure that the results are not influenced by the two-dimensionality of the flow (Schmalzl, Breuer & Hansen 2004) as in quasi-two-dimensional experiments (Xia, Sun & Zhou 2003) and two-dimensional numerical simulations (Sugiyama *et al.* 2010), we perform three-dimensional direct numerical simulations (DNS) of the turbulent flow within a cylindrical container with aspect ratio one. This geometry is used in many experiments because of its symmetry and certain experimental advantages. On the other hand this also introduces the disadvantage of the lack of asymmetries, which stabilise the large-scale circulation (LSC) for sufficiently large *Ra* and can simplify the analysis. Azimuthal re-orientations of the large-scale motion may occur in cylindrical containers as found in experiments (Cioni, Ciliberto & Sommeria 1997; Brown & Ahlers 2006; Resagk *et al.* 2006) and numerical simulations (Mishra *et al.* 2011; Stevens, Clercx & Lohse 2011*a*) as well.

To analyse the azimuthal orientations and to find a time period without major reorientations we use the method by Brown & Ahlers (2006). For such time periods

https://doi.org/10.1017/jfm.2012.69 Published online by Cambridge University Press

the analysis of the flow is reduced to a plane in which the LSC is mainly located. Therefore the analysed fields are two-dimensional while they still contain three-dimensional physics. A further analysis using different diagnostic functions shows that additional more complex modes like twisting (Funfschilling & Ahlers 2004; Funfschilling, Brown & Ahlers 2008) and sloshing (Xi, Zhou & Xia 2006; Xi *et al.* 2009; Zhou *et al.* 2009; Brown & Ahlers 2009) vanish statistically and do not disturb the time-averaged fields. To reduce the complexity of the wind analysis, the main focus is further on BLs occurring next to the heated bottom plate, namely along one line which is the wind direction. Besides its simplicity, this approach allows the comparison of the results with those of the two-dimensional PB theory.

The paper is organised as follows. In § 2 the numerical method and the simulation parameters are presented. Numerical results with respect to the Nusselt number are compared to experimental ones in § 3. Distributions of the local heat flux and the corresponding flow fields are also analysed there. In § 4 different procedures to determine the LSC plane within the cylindrical geometry and the proper time-averaging period are described and compared. To perform the BL analysis a method to investigate local instantaneous profiles is suggested and validated in § 5. Here the main focus is on how to determine the BL thickness and the corresponding quantities in detail. In § 6 this method is applied to flow fields for different Ra and mean characteristics of the wind and BLs are studied. In particular the scalings of the mean quantities with Ra are investigated. The results obtained are compared in § 7 with existing theoretical approaches. Finally the results are summarized in § 8.

2. Numerical method and setup

Direct numerical simulations (DNS) of turbulent Rayleigh–Bénard convection have been performed using a fourth-order-accurate finite-volume code in cylindrical coordinates (r, ϕ, z) together with semi-implicit time-integration as described in detail by Shishkina & Wagner (2005). The method was originally developed by Schmitt, Richter & Friedrich (1986) and is based on the volume-balance procedure by Schumann (1973), staggered grids and uses the Chorin ansatz for pressure–velocity coupling.

The dimensionless conservation laws of momentum, energy and mass in the Oberbeck–Boussinesq approximation with gravitational acceleration in the z-direction read:

$$\partial_t \boldsymbol{u} + \boldsymbol{u}\cdot\boldsymbol{\nabla}\boldsymbol{u} = -\boldsymbol{\nabla} p + \nu_1 \nabla^2 \boldsymbol{u} + T\boldsymbol{e}_z, \tag{2.1}$$

$$\partial_t T + \boldsymbol{u}\cdot\boldsymbol{\nabla} T = \nu_2 \nabla^2 T, \quad \boldsymbol{\nabla}\cdot\boldsymbol{u} = 0. \tag{2.2}$$

Here ∂_t stands for the partial derivative with respect to time t and $\boldsymbol{u}, T, p, \boldsymbol{e}_z$ denote the dimensionless velocity, temperature, dynamic pressure and unit vector in z-direction, respectively. The computational domain is a cylindrical container with aspect ratio $\Gamma = \widehat{D}/\widehat{H} = 1$ where $\widehat{D}$ stands for the diameter and $\widehat{H}$ for the height of the container, where the hat denotes a dimensional quantity. The equations are closed by the following set of boundary conditions: fixed temperatures on bottom and top plates, an adiabatic vertical wall and no-slip condition on all walls. If the cylinder diameter $\widehat{D}$ and the free-fall velocity $(\widehat{\alpha}\widehat{D}\widehat{g}\widehat{\Delta})^{1/2}$ are used as references for distance and velocity (while their ratio is the reference for the time), and the temperature is made dimensionless by $T = (\widehat{T} - \widehat{T}_M)/\widehat{\Delta}$, this yields parameters $\nu_1 = Pr^{1/2} Ra^{-1/2} \Gamma^{-3/2}$ and $\nu_2 = Ra^{-1/2} Pr^{-1/2} \Gamma^{-3/2}$. ($\widehat{\Delta}$ denotes the difference between

https://doi.org/10.1017/jfm.2012.69 Published online by Cambridge University Press

Ra	N_r	N_ϕ	N_z	n_T	$\check{n}_T$	n_u	$\check{n}_u$	Nu	τ
10^5	24	128	48	8	2	7	2	3.85(±0.02)	3776
3×10^5	48	256	96	10	2	10	2	5.82(±0.03)	682
10^6	48	256	96	8	3	7	3	8.6(±0.1)	690
3×10^6	96	256	192	11	3	10	3	11.95(±0.08)	993
7×10^6	96	256	192	9	3	9	3	15.2(±0.1)	1635
10^7	96	256	192	8	4	8	3	16.9(±0.2)	3775
3×10^7	192	512	384	16	4	14	4	22.8(±0.2)	515
7×10^7	192	512	384	12	5	11	4	29.0(±0.1)	586
10^8	192	512	384	11	5	11	5	31.9(±0.2)	1240
10^9	384	1024	768	13	7	12	6	63.1(±0.4)	318

TABLE 1. Simulation parameters for $Pr = 0.786$, $\Gamma = 1$: number of mesh nodes in the i-direction N_i $(i = r, \phi, z)$, number of nodes in the thermal/viscous BL as used in DNS (n_T/n_u) and as required by theory (Shishkina *et al.* 2010) $(\check{n}_T/\check{n}_u)$, the Nusselt number Nu with its maximal deviation and the number of dimensionless time units τ used for the averaging.

the temperatures of the bottom and top plates and $\widehat{T}_M$ their arithmetical mean value.) Therefore only the Rayleigh number $Ra = \widehat{\alpha}\,\widehat{g}\widehat{H}^3\widehat{\Delta}/\widehat{\nu}\,\widehat{\kappa}$, the Prandtl number $Pr = \widehat{\nu}/\widehat{\kappa}$ and the aspect ratio Γ occur as parameters fixing the set of equations. Note that in the Oberbeck–Boussinesq approximation material properties like the kinematic viscosity $\widehat{\nu}$, the thermal diffusivity $\widehat{\kappa}$, the thermal volume expansion coefficient $\widehat{\alpha}$ and the gravitational acceleration $\widehat{g}$ are constant and therefore their reference values are formally set to some value. (In the following the hat for dimensional quantities is omitted for simplicity.)

In order to perform a proper DNS, Kolmogorov and Batchelor scales need to be resolved, which requires a large number of computational nodes. For the globally averaged Kolmogorov length scale η_k the exact relation $\eta_k = Pr^{1/2}\,[Ra(Nu-1)]^{-1/4}$ holds and the Batchelor length scale η_T can be estimated via $\eta_T = \eta_k Pr^{-1/2}$. Since $Pr = 0.786 < 1$ in all our simulations, resolving the Kolmogorov length scale is the stronger requirement. As shown for example by Kunnen *et al.* (2008) the local Kolmogorov length scale η_k^{local} close to the rigid walls is much smaller than its spatial average η_k. Therefore the boundary layer region requires finer spatial resolution than the bulk region. Neglecting this might lead to wrong results even for integral quantities like the Nusselt number as was shown by Stevens *et al.* (2010). The required number of grid points in the boundary layers has been estimated by Shishkina *et al.* (2010). It is displayed in table 1 together with the actual number of nodes in the DNS. The spatially averaged Kolmogorov scale is used as the resolution requirement for the bulk region in every direction. Note that in this case the bulk resolution in our DNS is finer than is needed due to the inhomogeneous distribution of η_k^{local}.

To enable a statistical analysis, the flow motion is saved in two different ways. On the one hand an *a priori* time-averaging is performed. This means that for the whole domain time-averaged temperature and velocity fields together with higher moments and correlations are collected by sampling every 1.8×10^{-3}–3.5×10^{-3} time units (depending on Ra). On the other hand, to allow *a posteriori* time-averaging of different complex flow characteristics as well as an analysis of time histories, a complete instantaneous flow field (temperature and velocity) is saved about three times each dimensionless time unit.

https://doi.org/10.1017/jfm.2012.69 Published online by Cambridge University Press

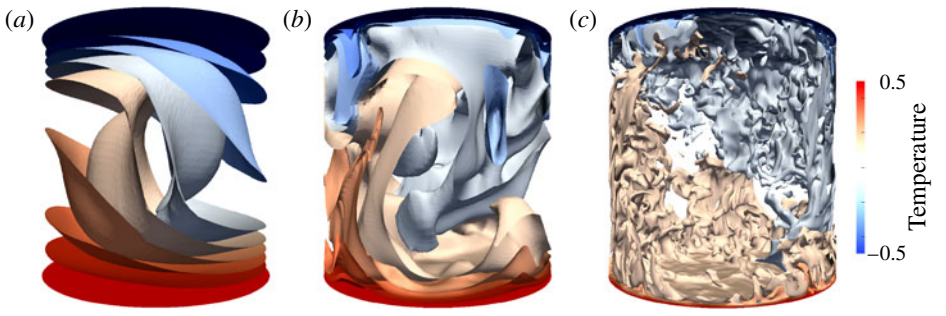


FIGURE 1. Instantaneous temperature iso-surfaces for (*a*) $Ra = 10^5$, (*b*) $Ra = 10^7$, and (*c*) $Ra = 10^9$; $Pr = 0.786$, $\Gamma = 1$.

As an example instantaneous temperature iso-surfaces obtained for three different Ra are shown in figure 1. Even though the mean flow is similar in all three cases (upflow on the left and downflow on the right) the shape of the iso-surfaces changes dramatically with Ra. Roughly speaking the size of the structures decreases rapidly with increasing Ra.

3. Local heat flux and Nusselt number

The heat flux $\boldsymbol{\Omega} = \boldsymbol{u}T - \kappa\boldsymbol{\nabla}T$ is the system's response to an imposed temperature gradient. Since the main interest lies in the heat transport from the hot bottom plate to the cold top plate, the vertical (z) component of the heat flux Ω_z is considered. It is made dimensionless with the vertical heat flux which would occur in a solid body with the same properties, resulting in $\Omega_z = \sqrt{\Gamma PrRa}\, u_z T - \Gamma^{-1}\partial_z T$. For comparison e.g. with experiments, an integral quantity, namely the Nusselt number $Nu = \langle \Omega_z \rangle_{t,\phi,r}$ is used. (Here $\langle Q \rangle_\xi$ denotes the average of the quantity Q with respect to the variable ξ.) It can be shown analytically and is well-known that Nu is independent of z. Thus the deviations of Nu for different heights can be used as a measure for reaching a statistically steady state. In table 1 the Nusselt numbers obtained are presented together with their maximal deviation from the z-averaged Nu.

In figure 2 the reduced Nusselt numbers $Nu/Ra^{0.3}$ from our DNS are compared to DNS and experiments from the literature. First of all it should be noted that our results cannot be expressed with a universal scaling exponent for the whole Ra-range considered, but there exist different regimes with a smooth transition: $Ra \lesssim 10^6$, $10^6 \lesssim Ra \lesssim 10^8$ and $Ra \gtrsim 10^8$. The latter observation is especially well supported by DNS results from the literature and the measurements by Ahlers *et al.* (2009*a*), with which a good agreement is found. The existence of the different regimes has already been reported in the literature (see Grossmann & Lohse 2001 and Ahlers *et al.* 2009*b*). The apparent differences in the results obtained by different authors can be partly explained by the variations in aspect ratios and Prandtl numbers. The remaining deviations to the measurements might be due to the different experimental setups and conditions, but this issue is one of the open problems in RBC (Ahlers *et al.* 2009*b*) and goes beyond the scope of the present paper.

Besides the integral vertical heat flux Nu, the spatial distribution of the local heat flux Ω_z is also worth investigating, since it is related to large-scale flow structures. In figure 3 the time-averaged distribution of the local heat flux (in units of the volume-averaged Nusselt number) on the top and bottom plates is presented. Due

https://doi.org/10.1017/jfm.2012.69 Published online by Cambridge University Press

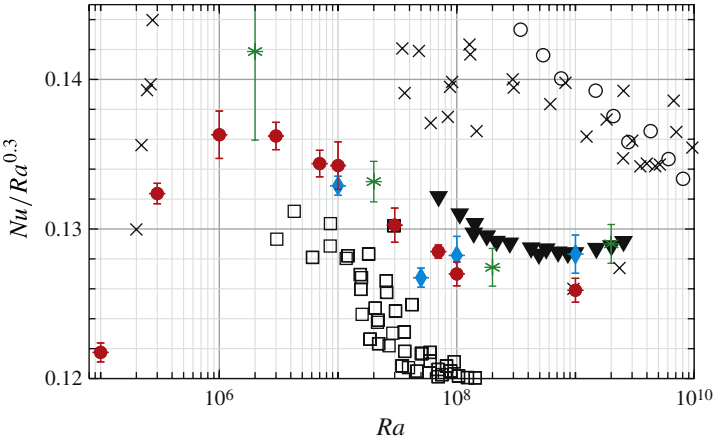


FIGURE 2. Comparison of reduced Nusselt numbers for different Ra from our DNS (red filled circles, $Pr = 0.786$, $\Gamma = 1$) with DNS results by Stevens *et al.* (2010) (green stars, $Pr = 0.7$, $\Gamma = 1/2$) and Bailon-Cuba, Emran & Schumacher (2010) (blue diamonds, $Pr = 0.7$, $\Gamma = 1$) as well as experimental results by Ahlers *et al.* (2009*a*) (black triangles, $Pr = 0.67$, $\Gamma = 1/2$), Roche *et al.* (2003) (black squares, $Pr = 0.82$–0.84, $\Gamma = 1/2$), Niemela & Sreenivasan (2003) (black open circles, $Pr = 0.68$–0.69, $\Gamma = 1/2$) and Chavanne *et al.* (2001) (black crosses, $Pr = 0.65$–0.76, $\Gamma = 1/2$).

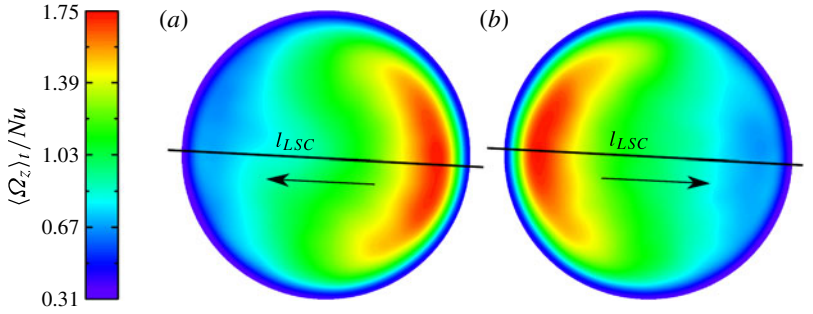


FIGURE 3. Time-averaged local heat flux $\langle \Omega_z \rangle_t$ in units of Nu on (*a*) the bottom and (*b*) the top plate. The plane of the large-scale circulation is marked with a solid black line l_{LSC} while the arrows point in the direction of the wind. $Ra = 10^7$, $Pr = 0.786$, $\Gamma = 1$.

to the no-slip conditions this is just a multiple of the vertical temperature gradient. From figure 3 it is obvious that there is one preferred direction marked with a black line labelled l_{LSC}, which is an axis of symmetry and which can be interpreted as the direction of the large-scale circulation.

If we select the vertical cross-section of the flow field through l_{LSC}, i.e. what we interpret as the plane of the large-scale circulation, we obtain figure 4(*a*) in which Ω_z (colour) together with the velocity vectors are shown for $Ra = 10^7$. In addition the flow field in the plane orthogonal to the LSC is visualized (figure 4*b*). For details regarding the averaging procedure and the extraction of the LSC plane see § 4. In the LSC plane the LSC itself represents a huge vortex structure with a diagonal adjustment and two smaller counter-rotating vortices in the upper left and lower right corner. The local

https://doi.org/10.1017/jfm.2012.69 Published online by Cambridge University Press

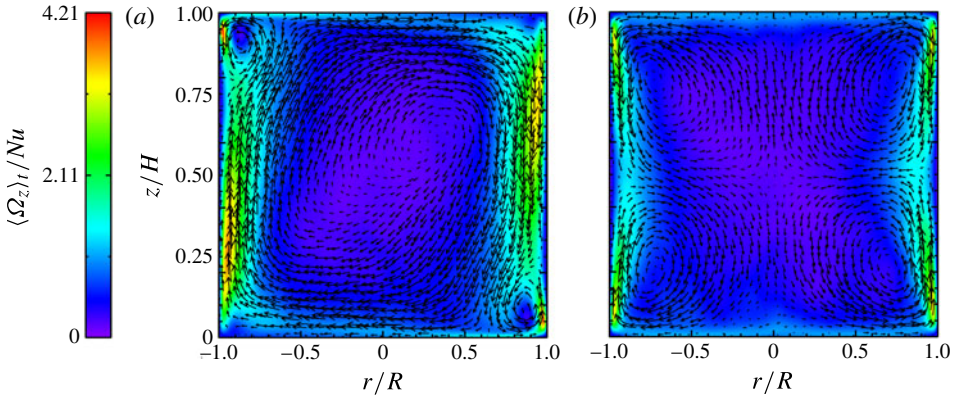


FIGURE 4. Time-averaged local heat flux (colour) in units of the Nusselt number and velocity (vectors) in the plane of (*a*) the LSC and (*b*) orthogonal to it, $Ra = 10^7$, $Pr = 0.786$, $\Gamma = 1$.

heat flux increases in the vicinity of the vertical wall. This has also been reported by Shishkina & Wagner (2007). Within this region the heat flux is largest close to the smaller vortices. We assume therefore that these small structures are essential for the global heat transport. This argument is also supported by figure 3 in which the largest vertical heat flux on the bottom plate is again located in the region of the counter-rotating vortex.

In the central vertical cross-section orthogonal to the LSC (see figure 4*b*) there are four vortices of almost the same size rotating in different directions. In the horizontal direction at half-height the fluid moves towards the centre and at the cylinder axis the flow divides into an upward and downward motion. These observations agree well with the four-roll structure experimentally measured by Sun, Xia & Tong (2005). Again the strongest vertical heat flux is located close to the vertical wall. It is surprising that even though the velocity field shows a completely different behaviour in the two orthogonal planes, the resulting heat flux distribution in both planes is quite similar, whereas there is an up–down symmetry which cannot be found in the LSC plane.

4. Extraction of the LSC plane

In a cylindrical domain the LSC can perform azimuthal reorientations up to complete reversals. This means that in order to study the LSC in a cylindrical container in detail, a time interval without reorientations of the LSC must be identified. It is obtained by following the method proposed by Brown & Ahlers (2006) which has also been used to analyse DNS data by Mishra *et al.* (2011) and Stevens *et al.* (2011*a*).

The temperature on the vertical wall at half the cylinder height is fitted with the (discrete) function $\psi(x_i) = A\cos((2\pi \mathrm{i}/N_\phi) + \phi_{LSC})$ using all N_ϕ azimuthal nodes at the positions x_i. This is done for all samples saved during the runtime (three per time unit as described above). One obtains the time histories of the amplitudes A and the phase shifts ϕ_{LSC}, shown in figure 5 as an example for $Ra = 10^9$.

If a certain time period is characterized by a phase shift ϕ_{LSC} which varies within the interval $\langle \phi_{LSC} \rangle_t \pm \pi/6$, we consider it as a time period without reorientations. Note that even in such time periods spikes of $\phi_{LSC}(t)$ can occur. It was shown by Stevens

https://doi.org/10.1017/jfm.2012.69 Published online by Cambridge University Press

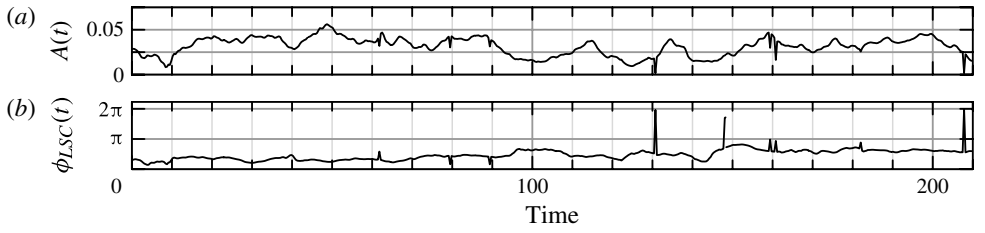


FIGURE 5. Time history of the fitting parameters: (*a*) amplitude $A(t)$ and (*b*) phase shift $\phi_{LSC}(t)$ for $Ra = 10^9$, $Pr = 0.786$, $\Gamma = 1$ in a time interval without reorientations, i.e. within the interval $\langle\phi_{LSC}\rangle_t \pm \pi/6$.

Ra	3×10^6	10^7	10^8	10^9
t_{max}	602	634	682	210

TABLE 2. Length of time intervals (t_{max}) without reorientations for different Ra as used for analysis of the LSC.

et al. (2011*a*) that these spikes are caused by single plumes and can be avoided in the time series by averaging over a small number of samples. Since we are not interested in the time series of ϕ_{LSC} at this point but just want to determine proper time intervals without reorientations, we simply neglect these spikes. For the time periods obtained it is possible to analyse the LSC from time-averaged fields. The advantage of this method is its simplicity since the analysis uses two-dimensional fields but still represents the nature of three-dimensional physics.

In table 2 the time interval lengths t_{max} without reorientations, used in the LSC analysis, are presented for different Ra. Optimal time intervals might be longer than those used in our analysis and are to be investigated in the future. Note that for Ra below 3×10^6 either the flow is stationary or no proper period could be found as many reorientations occur. The latter leads to very short time intervals between reorientations, so that it is impossible to obtain converged statistics. Throughout the paper (except for the Nu analysis) the fields are averaged over the described time periods without reorientations. The plane of the LSC is thereby fixed by the angle $\langle\phi_{LSC}\rangle_t$ which we call ϕ_{LSC} for simplicity in the following. Note that our LSC plane does not coincide with the time average of the instantaneous LSC planes obtained by using the method of Brown & Ahlers (2006). The latter approach to extract the LSC is more sensitive to disturbances due to the appearance of strong single plumes (see e.g. Stevens *et al.* 2011*a*) as it is illustrated for example by the spikes in figure 5(*b*).

Besides the reorientations, the LSC can perform much more complex movements. These include off-centre (sloshing) modes (Xi *et al.* 2006, 2009; Zhou *et al.* 2009; Brown & Ahlers 2009) as well as twisting (Funfschilling & Ahlers 2004; Funfschilling *et al.* 2008), which cannot be fully detected by the method of Brown & Ahlers (2006). Therefore we perform an additional analysis to determine whether these modes influence the time-averaged fields. For this purpose we consider five functions $f_i(\phi)$ to determine ϕ_{LSC} from time-averaged fields in five different ways. These functions reflect the flow dynamics in different regions of the domain. If additional modes (like

https://doi.org/10.1017/jfm.2012.69 Published online by Cambridge University Press

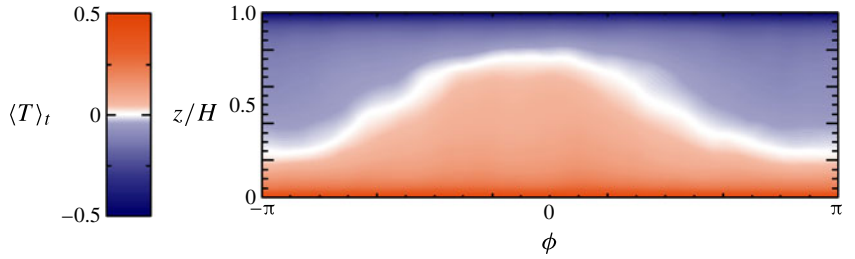


FIGURE 6. Time-averaged temperature on the vertical wall. $Ra = 10^7$, $Pr = 0.786$, $\Gamma = 1$.

sloshing or twisting) influence the dynamics in that region, it should lead to a different azimuthal behaviour of these functions.

We have already seen in figure 3 that ϕ_{LSC} can be determined from the local heat flux on the bottom plate. More quantitatively, we analyse its rescaled radial average

$$f_{\Omega_z}(\phi) = \frac{2\,\langle\Omega_z\rangle_{t,r,z=0} - (\max(\langle\Omega_z\rangle_{t,r,z=0}) + \min(\langle\Omega_z\rangle_{t,r,z=0}))}{\max(\langle\Omega_z\rangle_{t,r,z=0}) - \min(\langle\Omega_z\rangle_{t,r,z=0})}, \tag{4.1}$$

which is a function with values within $[-1{:}1]$. A maximum is expected for ϕ_{LSC} and a minimum for $\phi_{LSC} + \pi$. In between we expect a smooth crossover to end up with a continuous graph.

Besides the heat flux, the ϕ-component of the vorticity, i.e. $\omega_\phi = (\boldsymbol{\nabla} \times \boldsymbol{u}) \cdot \boldsymbol{e}_\phi$ seems to be a characteristic quantity as figure 4 suggests. By averaging in radial and vertical directions this is reduced to a function $f_\omega(\phi)$, namely

$$f_\omega(\phi) = \frac{2\,\langle\omega_\phi\rangle_{t,r,z} - (\max(\langle\omega_\phi\rangle_{t,r,z}) + \min(\langle\omega_\phi\rangle_{t,r,z}))}{\max(\langle\omega_\phi\rangle_{t,r,z}) - \min(\langle\omega_\phi\rangle_{t,r,z})}. \tag{4.2}$$

For ϕ_{LSC} we expect a high absolute value of the integral vorticity component $\langle\omega_\phi\rangle_{t,r,z}$ while for $\phi_{LSC} + \pi/2$ the counter-rotating vortices cause an integral vorticity close to zero.

An interesting feature of the LSC is its footprint on the vertical wall. First we consider the temperature on the vertical wall shown in figure 6. We are interested in the vertical position z_0 at which the mean temperature is reached. This results in a rescaled function

$$f_T(\phi) = \frac{2z_0 - (\max(z_0) + \min(z_0))}{\max(z_0) - \min(z_0)}. \tag{4.3}$$

Due to rising/falling of warm/cold plumes, which constitute in organised form the LSC, the mean temperature can be found closer to the top plate for ϕ_{LSC} and closer to the bottom plate for $\phi_{LSC} + \pi$. In figure 6 a cosine-like behaviour of $z_0(\phi)$ is visible.

Besides the temperature footprint the LSC induces the wall shear stress on the vertical wall shown in figure 7. The absolute wall shear stress $\tau_w^{total} = \sqrt{\langle\partial_r u_z\rangle_t^2 + \langle\partial_r u_\phi\rangle_t^2}$ is displayed by colours and its components due to vertical motion $\langle-\partial_r u_z\rangle_t$ and azimuthal motion $\langle-\partial_r u_\phi\rangle_t$ as vectors. Again a cosine-like (blue) curve is obtained. This time the curve reflects the vertical position of the stagnation point z_s as a function of the angle ϕ and therefore we define the next indicating function as

$$f_\tau(\phi) = \frac{2z_s - (\max(z_s) + \min(z_s))}{\max(z_s) - \min(z_s)}. \tag{4.4}$$

https://doi.org/10.1017/jfm.2012.69 Published online by Cambridge University Press

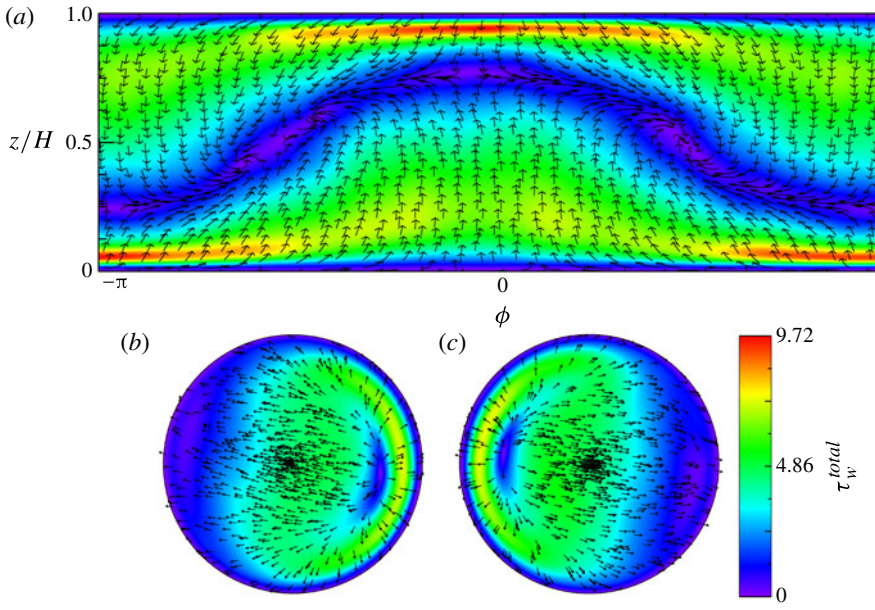


FIGURE 7. Absolute (colour) τ_w^{total} and contributions of different directions of movement (vectors) of the time-averaged wall shear stress on the (*a*) vertical wall, (*b*) bottom plate and (*c*) top plate. $Ra = 10^7$, $Pr = 0.786$, $\Gamma = 1$.

Finally, we consider the temperature distribution on the vertical wall at half-height as in the fitting procedure described at the beginning of this section. We expect to find a cosine function in the time-averaged fields, since it was already used as a fitting function for instantaneous fields. Thus the fifth function reads

$$f_{T_c}(\phi) = \frac{2\,\langle T\rangle_{t,r=R,z=H/2} - (\max(\langle T\rangle_{t,r=R,z=H/2}) + \min(\langle T\rangle_{t,r=R,z=H/2}))}{\max(\langle T\rangle_{t,r=R,z=H/2}) - \min(\langle T\rangle_{t,r=R,z=H/2})}. \tag{4.5}$$

To complete the analysis of the different functions indicating the angle ϕ_{LSC}, we present them together in figure 8. One can see that the five functions based on flow footprints on the bottom plate (f_{Ω_z}), on the vertical walls (f_τ, f_T, f_{T_c}) and integral characteristics (f_ω) almost coincide. Therefore a characteristic ϕ-behaviour of these quantities exists and reflects almost the same ϕ_{LSC}. Such a collapse of different quantities in a turbulent flow can be present only if any additional modes like sloshing or twisting vanish statistically for the considered Ra, Pr, Γ.

If only a short time period is available (for example due to frequent reorientations of the LSC or high computational costs for DNS) it is interesting to investigate, which of the considered ϕ-functions that indicate ϕ_{LSC} converges faster. In figure 9 the relative deviation in the L^2-norm from the final curve is shown as a function of the length of the averaging period. The relative deviation σ of a quantity Q depending on a variable ξ from a reference Q_{ref} is calculated via

$$\sigma = \sqrt{\frac{\int \left[Q(\xi) - Q_{ref}(\xi)\right]^2 \mathrm{d}\xi}{\int \left[Q_{ref}(\xi)\right]^2 \mathrm{d}\xi}} \tag{4.6}$$

https://doi.org/10.1017/jfm.2012.69 Published online by Cambridge University Press

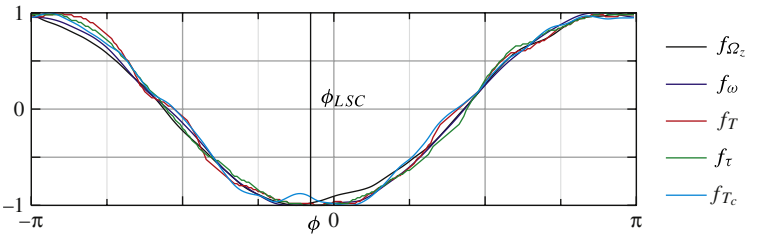


FIGURE 8. Different functions indicating the LSC based on: f_{Ω_z}, the local heat flux on the bottom plate (4.1); f_ω, the azimuthal component of the vorticity (4.2) in central vertical cross-sections; f_T, the height at which the arithmetical mean temperature on the vertical wall is reached (4.3); f_τ, the height of the stagnation point (4.4) at the vertical wall; and f_{T_c}, the temperature on the vertical wall at $z = H/2$ (4.5), $Ra = 10^7$, $Pr = 0.786$, $\Gamma = 1$.

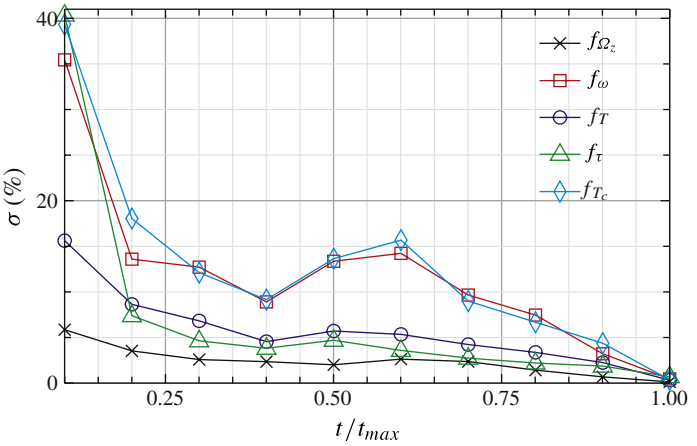


FIGURE 9. Convergence of different quantities with increasing averaging period. $Ra = 10^7$, $Pr = 0.786$, $\Gamma = 1$.

and can interpreted as a prediction error with respect to an insufficient averaging time. Note that even for the maximal averaging time t_{max} zero is not necessarily reached as the reference is calculated from time-averaged fields with a higher sampling rate (as described at the end of § 2). From figure 9 it is concluded that the function f_{Ω_z} based on the local heat flux on the bottom plate provides almost immediately the direction of the LSC with an error of ∼6 % while the method by Brown & Ahlers (2006) (f_{T_c}) predicts ϕ_{LSC} at that time with an error of ∼ 40 %. From the latter we conclude that if only a short time interval or a set of few samples is available for determining ϕ_{LSC} (for the above-mentioned reasons), the heat flux criterion should be favoured. It is of course applicable only to numerical data as measuring the local heat flux on the whole plate in experiments is not yet possible. In measurements the available time for averaging is often much larger than that in numerical simulations, and therefore the method by Brown & Ahlers (2006) is preferable in this case.

From figure 9 it is obvious that within the time interval considered additional dynamics occur around $t/t_{max} = 0.6$. This leads to a disturbance of the functions f_{T_c}

https://doi.org/10.1017/jfm.2012.69 Published online by Cambridge University Press

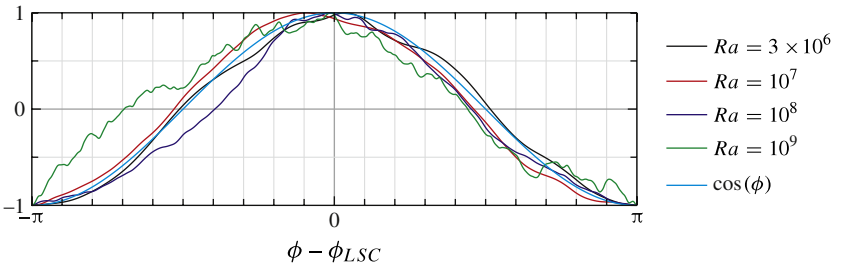


FIGURE 10. Function f_{Ω_z} (local heat flux on the bottom plate, averaged in time and radial direction) shifted in the ϕ-direction for different Ra and the cos-function for comparison.

and f_ω near $t/t_{max} = 0.6$, which only influences the speed of convergence but not the time-averaged field as shown in figure 8. To check whether the ϕ-dependence of the time-averaged field is universal within a certain interval of Ra (and fixed Pr, Γ), we consider the heat flux criterion mentioned above. In figure 10 the comparison of the function f_{Ω_z} (of course shifted in ϕ to offset different orientations of the LSC in the different simulations) with a cosine function reveals a good agreement for different Ra. This shows that there is a universal behaviour of time-averaged fields if no LSC reorientation takes place within the averaging period. Moreover the similarity obtained with the cosine function is an indirect justification for the fitting procedure described at the beginning of the section.

In addition to the above-mentioned quantities the LSC of course also causes wall shear stress on the top/bottom plate, which is presented in figures 7(*b*) and 7(*c*). Colours display the absolute wall shear stress

$$\tau_w^{total} = \sqrt{\langle \partial_z u_r \rangle_t^2 + \langle \partial_z u_\phi \rangle_t^2}$$

and vectors its components due to radial motion $\langle \pm \partial_z u_r \rangle_t$ and azimuthal motion $\langle \pm \partial_z u_\phi \rangle_t$. Comparing this with the wall shear stress on the vertical wall, we conclude that the LSC is formed mainly by the radial and vertical motion at the top/bottom and vertical walls, respectively.

If we reduce our analysis to the plane of the LSC, we consider the specific case where one velocity component is responsible for the wall shear stress and the viscous BL. Even more interesting are the distributions on the horizontal walls, since there a thermal BL develops in addition to the viscous one. We concentrate our analysis on the region close to the bottom plate knowing that the situation is similar on the top plate due to symmetry.

5. Boundary layer analysis

In the following a step-by-step method to extract and analyse the local boundary layer thickness from instantaneous flow fields is introduced and discussed.

5.1. *Definition*

To evaluate the boundary layer thickness close to the heated bottom plate, it is necessary to deal with instantaneous flow fields. Time-averaged fields do not provide the correlations which are required for our BL analysis. One can use different definitions of the BL thickness, such as the fluctuation criterion (boundary layer thickness is defined as the position of the maximum of the temperature/velocity

https://doi.org/10.1017/jfm.2012.69 Published online by Cambridge University Press

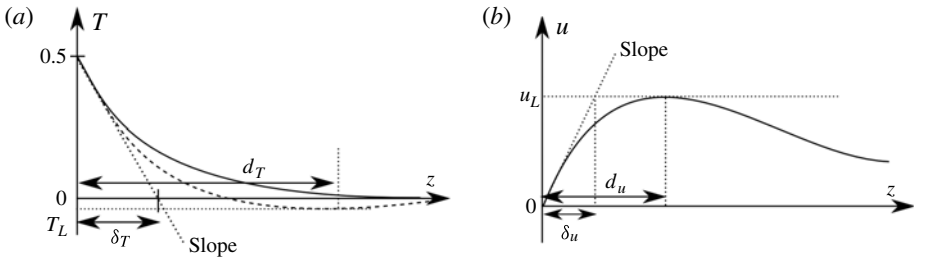


FIGURE 11. Definition and nomenclature for BL thicknesses and associated quantities for the cases of (*a*) thermal and (*b*) viscous boundary layers.

fluctuations), which lead in general to different results. We use the well-known and often applied (e.g. Shishkina *et al.* 2010) slope criterion defined in figure 11 because it is also applicable locally to instantaneous flow fields.

To apply this criterion the slope of the temperature or (radial) wind velocity is evaluated at the wall. The thermal or viscous boundary layer thickness is then defined as the height z at which the slope straight line crosses a temperature or velocity level T_L or u_L, respectively. The levels of the quantities correspond to the dotted horizontal lines in figure 11.

As demonstrated in figure 11, the analysis of the thermal BL is similar but not identical to that of the viscous BL. The reason for this is the different boundary conditions for the two quantities. Since the temperature is always maximal at the bottom, the slope at this wall is always negative. On the contrary the velocity (we call it simply u here but mean the radial velocity within the fixed plane of the LSC) is vanishing at the wall due to the no-slip condition allowing generally negative as well as positive slopes. In summary two quantities are needed to determine the BL thickness: the slope and the level.

In general the temperature level obtained from instantaneous flow fields differs from the arithmetical mean temperature (here zero) and can be negative or positive. In figure 11(*a*) an example of the negative temperature level T_L at position d_T is sketched. It is therefore necessary to determine a level for the case of thermal BLs also since only the mean temperature distribution might lead to a wrong thermal BL thickness. This has also been shown by Zhou *et al.* (2010). To determine the thermal BL thickness we use the global minimum of the temperature field within a certain z-interval I as the level value.

For the viscous BL the situation is even more tricky. As negative as well as positive slopes might occur, we have to consider positive and negative levels. Thus we need the global maximal as well as global minimal velocity value within I. The sign of the derivative which determines the slope should then fix the sign of the level quantity.

The length of the interval I is a free parameter in the definition of the proper temperature/velocity level. We will further analyse what influence the choice of I has on the resulting boundary layer thickness. If proper slopes and levels are provided a complete statistical analysis of the local boundary layer thickness can be performed.

In order to analyse the boundary layer on the bottom plate and corresponding quantities with special emphasis on the LSC, not all radial positions must be taken into account, since smaller structures that occur in the corners are not part of the LSC itself (see figure 4). As the position of the zero time-averaged wall shear stress

https://doi.org/10.1017/jfm.2012.69 Published online by Cambridge University Press

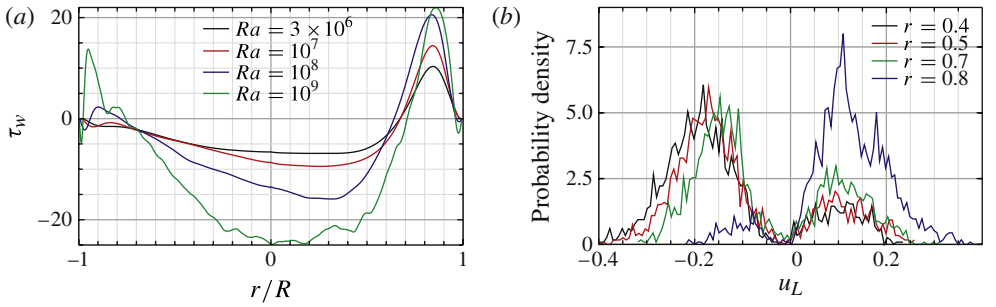


FIGURE 12. (*a*) Time-averaged wall shear stress $\tau_w = \langle \partial_z u \rangle_t$ on the bottom plate along l_{LSC} for different Ra and (*b*) p.d.f. of the velocity level u_L at different radial positions for $Ra = 10^7$, $Pr = 0.786$, $\Gamma = 1$.

(i.e. the mean stagnation point) is almost independent of Ra (as shown in figure 12*a*), we conclude that considering the region $J = \{r | r \in [-0.7 : 0.5]\}$ is sufficient. An argument for the upper bound can be found in figure 12(*b*). There the dependence of the probability density function (p.d.f.) for the maximal value of the radial velocity component in the lower half of the cell on the radial position is presented. It can be seen that mainly negative velocity values, which correspond to the wind velocity, occur for $r \leqslant 0.5$, while for larger r the positive velocity values, which are part of the smaller vortex in the corner, dominate. A similar argument can be made for the lower bound. During the following analysis we therefore concentrate on p.d.f.s in the region $l_{LSC} \cap J$.

5.2. *Determination of proper slopes and levels for the BL extraction*

In the following we compare different techniques for determining the thermal (δ_T) and viscous (δ_u) BL thicknesses, respectively. As described above, two main ingredients are necessary: the slope and the level. We focus on each of them separately and then combine them to evaluate the BL thickness.

First we address the question of how the slope can be extracted from a fluctuating instantaneous field. To answer this, we must decide whether the normal gradient at the wall is a good estimate of the slope or an additional fitting is needed. Since $\langle \partial_z f \rangle_t = \partial_z \langle f \rangle_t$ for a quantity $f \in \{T, u\}$, the slopes obtained from time-averaged fields can be used to check various differentiation techniques applied to instantaneous fields while evaluating the BL thickness. On the one hand we simply consider the derivative at the wall $\langle \partial_z f \rangle_t$ (fitted with a three-point Lagrange polynomial) as in the case of the time averaged fields $\partial_z \langle f \rangle_t$. On the other hand we take a number n_z of points next to the wall and perform a linear regression (with one free parameter as the value at the wall is fixed by the boundary condition). In figure 13 the comparison for different n_z and the derivative is shown for $Ra = 10^7$. We conclude that the direct derivative technique, i.e. $\langle \partial_z f \rangle_t$, delivers the best agreement with the time averaged field $\partial_z \langle f \rangle_t$ for both BLs, therefore it is applied for the BL extraction. The fact that fitting with a higher number of points leads to gentler slopes can be explained as follows: with increasing number of points the instantaneous vertical profiles deviate more from the linear ones, therefore their linear fits become gentler.

Besides the slope we also need a proper level and thus, as described above, an interval I in which it is determined. We know from theory that $\delta_T = H/(2Nu)$ is

https://doi.org/10.1017/jfm.2012.69 Published online by Cambridge University Press

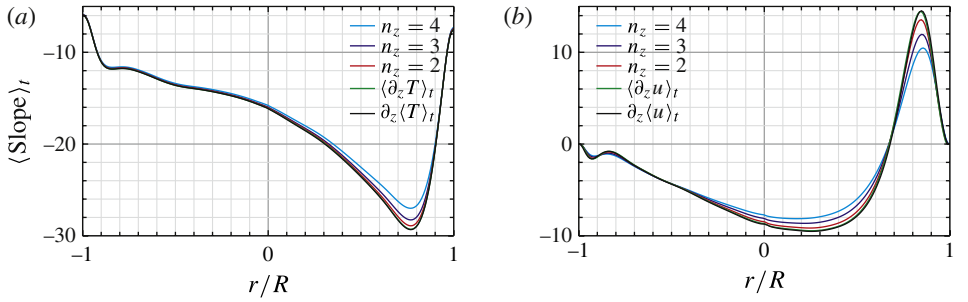


FIGURE 13. Different methods to obtain the (time averaged) slope of the (a) temperature field and (b) radial velocity field using linear fitting for the first n_z nodes and direct derivative $\langle\partial_z f\rangle_t$ compared to the time averaged field $\langle\partial_z f\rangle_t, f \in \{T, u\}$, $Ra = 10^7$, $Pr = 0.786$, $\Gamma = 1$.

a good approximation of the mean thermal BL thickness. In addition $\delta_T/\delta_u \approx 1$ holds for a Prandtl–Blasius BL for $Pr \approx 1$. Therefore we choose $I_n = nH/(2Nu)$ and compare the results obtained for different n. In addition we consider $I_\infty = H/2$ as a possible interval. As taking the maximum/minimum and time-averaging do not commute, we do not expect that the averaged results from instantaneous fields coincide with the results from the averaged field. Nevertheless in figure 14 in addition to the instantaneous results, also the results obtained for the averaged fields (with T_L and u_L within I_∞) are compared. Besides the levels reached, the position at which the maximum/minimum occurs is an interesting quantity. Therefore in figure 14(e,f) the p.d.f.s of the level values and boundary layer thicknesses obtained for different I are shown for the thermal and viscous cases.

We observe that the thermal BL analysis is much more sensitive to the size of the interval I. Since we want to develop one criterion for both types of BL, we derive it for the thermal BL and afterwards apply it to the viscous BL, as well. Negative temperature levels T_L sketched in figure 11(a) are typical for instantaneous temperature profiles. Indeed figure 14(a) reflects that for larger intervals the time-averaged temperature decreases. Figure 14(c) underlines this since with increasing size of I the p.d.f. sets the weight to negative velocity values instead of positive ones. This can be justified from figure 14(e) where additionally to the peaks at $d_T \approx 0.025$ a second peak at the upper bound of each considered interval is seen. This is due to events for which the global minimum occurs at the upper boundary. Since this peaks get less important for larger I for more events, the global minimum is found within the interval. Since we are interested in the level to define the BL thickness the first peak at $d_T \approx 0.025$ is the relevant one. If in the bulk at larger heights z a cold plume causes negative temperature values which in turn cause a lower T_L, this indeed should have minor influence on the BL thickness. Thus we decided that I_4 is the proper interval to evaluate the BL thicknesses as the main peak is already within this interval and it stretches not too deeply into the bulk region.

From figure 14(d) it is concluded that the velocity levels show a strong splitting due to the sign of the velocity. Since we are interested in the wind velocity of the LSC, the negative velocity values are of most interest to us. The peak in the p.d.f. close to zero (but on the positive side) is a result of the velocity fluctuations close to the wall (Zhou *et al.* 2011). Even if the peak is quite high this case can be neglected due to the small histogram bin size and therefore small probability.

https://doi.org/10.1017/jfm.2012.69 Published online by Cambridge University Press

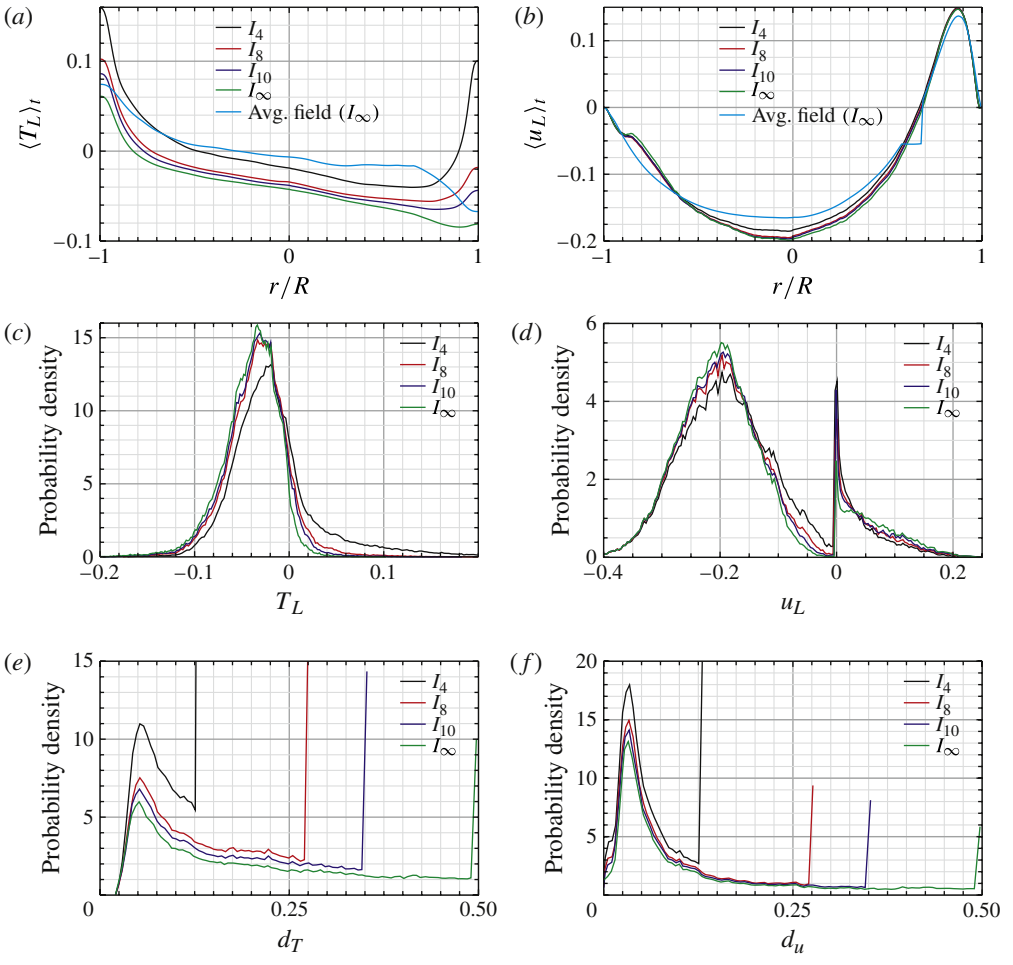


FIGURE 14. Evaluation of the temperature and velocity levels from searching within different z-intervals I. Time-averaged results for temperature (a) and velocity (b), corresponding p.d.f.s of the temperature (c) and velocity (d) for $r \in [-0.7, 0.5]$ and p.d.f.s for the height d at which the level is reached for the temperature (e) and velocity (f), $Ra = 10^7$, $Pr = 0.786$, $\Gamma = 1$.

5.3. *Resulting boundary layer thicknesses*

In figure 15 the BL thicknesses based on the obtained slopes and levels are presented. The fact that the p.d.f.s for different I are similar underlines that the choice of I (of course within proper bounds) has no major influence on the p.d.f. (and thus also not on the mean values) of the BL thickness.

The p.d.f. found for δ_u shows a similar behaviour as already reported by Zhou & Xia (2010) who conducted quasi-two-dimensional experiments and obtained (spatially averaged) BL profiles using particle image velocimetry (PIV). The p.d.f. rises strongly for small boundary layer thicknesses, reaches its maximum and descends much more slowly for larger BL thicknesses. The p.d.f. for the thermal BL behaves in a similar way but is wider and shifted to larger BL thicknesses. This will be discussed in detail in the next section.

https://doi.org/10.1017/jfm.2012.69 Published online by Cambridge University Press

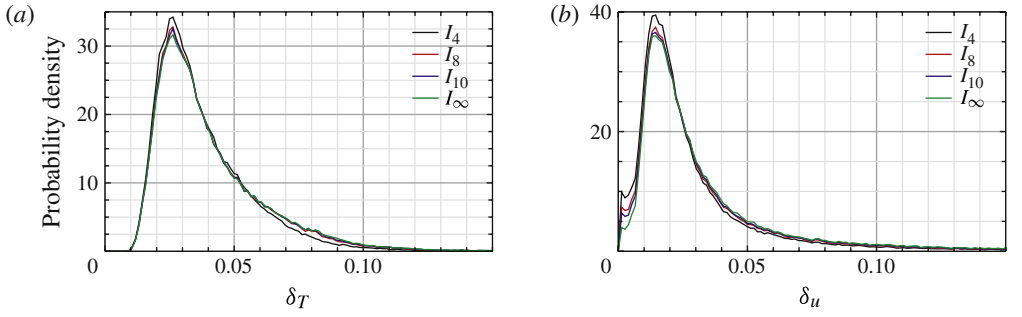


FIGURE 15. P.d.f.s of the obtained BL thicknesses of the (*a*) thermal BL and (*b*) viscous BL from searching within different z-intervals I for $r \in J$, $Ra = 10^7$, $Pr = 0.786$, $\Gamma = 1$.

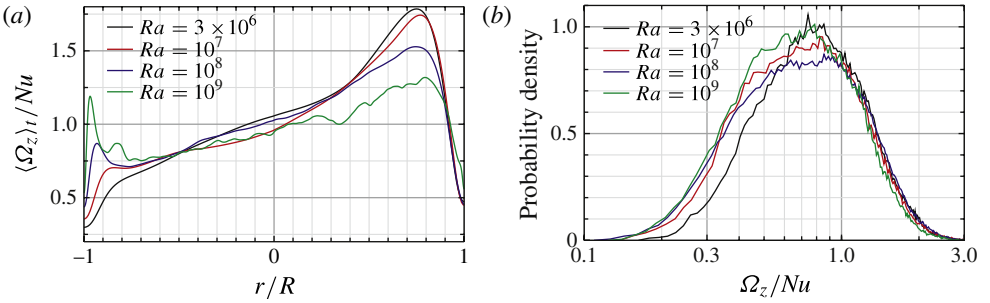


FIGURE 16. Local heat flux in units of Nu on the bottom plate along l_{LSC} for different Ra, (*a*) time-averaged and (*b*) p.d.f. for $r \in [-0.7, 0.5]$, $Pr = 0.786$, $\Gamma = 1$.

6. Boundary layer characteristics

The analysis of the Ra-dependence of BL characteristics includes the different quantities involved. Therefore the levels and slopes as well as the resulting BL thicknesses and their ratio are discussed.

6.1. *Slopes and levels*

As mentioned before the slopes of the temperature and wind velocity profiles are worth evaluating not only with respect to the BL thicknesses but because they are meaningful in themselves, as well. In the case of the temperature field the slopes at the wall are proportional to the local heat flux orthogonal to the wall. In the case of the bottom plate the slopes are thus proportional to the vertical local heat flux Ω_z.

In figure 16(*a*) the local heat flux along the wind direction is depicted in terms of Nu. It is observed that the heat flux normalized with Nu almost collapses for all Rayleigh numbers considered in the interval $J = \{r | r \in [-0.7, 0.5]\}$. In particular the maxima of the p.d.f.s of this local heat flux in the interval J occur for all Rayleigh numbers at $\sim$0.8 as shown in figure 16(*b*).

Outside J and close to the vertical wall the heat flux reflects some interesting features due to the secondary rolls as displayed in figure 16(*a*). From this we conclude that the vortices in the corners (here close to $r = 0.8$) are also essential drivers of the heat. The comparison of the horizontal normalized heat flux profiles for different Ra in

https://doi.org/10.1017/jfm.2012.69 Published online by Cambridge University Press

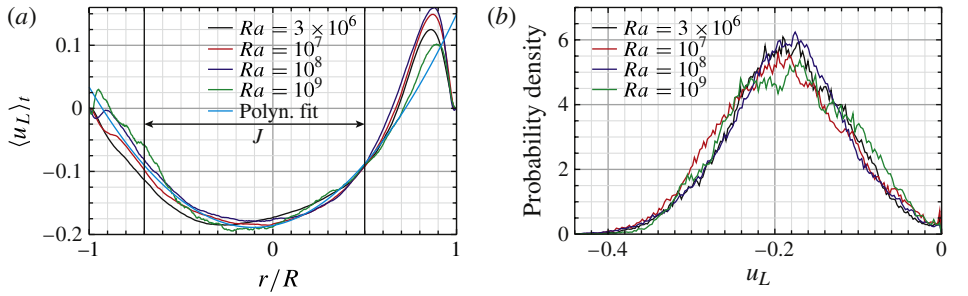


FIGURE 17. (*a*) Time-averaged wind velocity level u_L along l_{LSC} for different Ra with a polynomial fit for $r \in [-0.7, 0.5]$; (*b*) p.d.f. for the wind velocity level for $r \in [-0.7, 0.5]$, $Pr = 0.786$, $\Gamma = 1$.

figure 16(*a*) also shows that even though the largest Ω_z values are reached within this corner region for all the Ra, it becomes less important for increasing Ra.

Contrary to this another structure becomes more important for the heat flux with increasing Ra. It was shown in figure 12(*a*) that in the remaining corners (here close to $r = -0.9$) a smaller vortex structure develops. Owing to the rising plumes close to the vertical wall, the flow detaches from the bottom plate. For higher Ra this effect becomes so strong that a separation bubble and therefore a vortex structure develops, which induces motion against the direction of the wind close to the bottom plate and thus a positive τ_w.

This argument is also supported by the levels presented in figure 17(*a*) which for larger Ra reflect positive mean velocities in this corner region close to $r = -0.9$. Within J, where the wind is dominant, the mean velocity levels can be approximated by a parabola for all Ra considered. In figure 17(*a*) the fit with a second-order polynomial for $r \in J$ results in $u_L(r) = 0.277\,(r + 0.104)^2 - 0.189$. This means that the wind along the plate has a varying magnitude and reaches its maximum at $r = -0.104$. The existence of a varying wind velocity has been also observed by Zhou *et al.* (2011) in two-dimensional DNS and similarly by Kaczorowski *et al.* (2011) in DNS in a cube.

The observed Ra-independence of the dimensionless wind velocity magnitude is also visible in the p.d.f.s (see figure 17*b*). They almost coincide for all investigated Ra and are symmetric around $u_L \approx -0.2$. Similar results were obtained in experiments. For example du Puits *et al.* (2009) found a mean velocity magnitude of $|u_L| \approx 0.18$ in the centre of their cylindrical cell for $Ra = 1.12 \times 10^{11}$, $Pr = 0.7$ and $\Gamma = 1.13$, while Sun *et al.* (2008) obtained $|u_L| \approx 0.1$ in their quasi-two-dimensional experiments for $Ra = 3.43 \times 10^9$, $Pr = 4.3$ and $\Gamma = 1.04$. The deviation of our results from the latter might be an effect of the considerably different Prandtl numbers.

Besides the velocity levels the temperature levels T_L also reveal an interesting Ra-dependence. Their time averaged distributions and p.d.f.s are presented in figure 18. As shown by Zhou *et al.* (2010), the fluctuating temperature level has an effect on the p.d.f. of the thermal BL thickness. We have argued that levels below zero are reached due to a global temperature minimum within the interval I (recall figure 11). From figure 18 it is concluded that the radial distribution of the time averaged levels as well as the p.d.f. are shifted to higher levels, i.e. closer to the arithmetic mean temperature zero, with increasing Ra. Thus for higher Ra the case of a global temperature minimum which deviates from zero is less probable. If the temperature

https://doi.org/10.1017/jfm.2012.69 Published online by Cambridge University Press

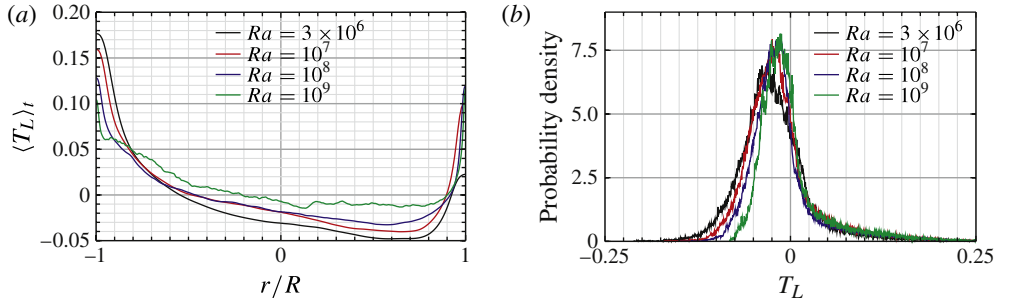


FIGURE 18. Temperature level T_L along l_{LSC} for different Ra, (a) time-averaged and (b) p.d.f. for $r \in [-0.7, 0.5]$, $Pr = 0.786$, $\Gamma = 1$.

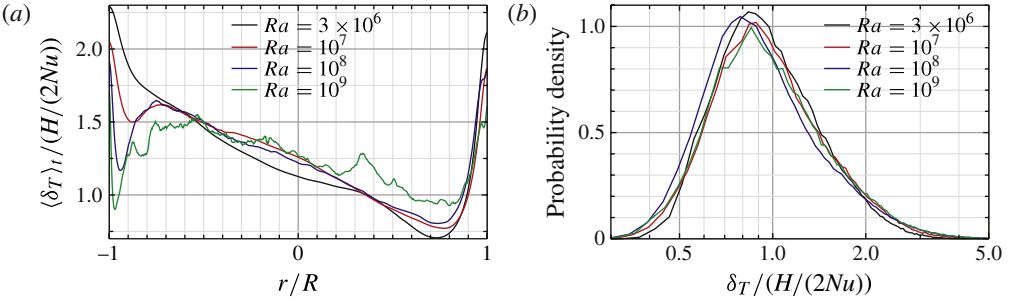


FIGURE 19. Thermal boundary layer thickness δ_T in units of $H/2Nu$, (a) time-averaged and (b) p.d.f. for $r \in [-0.7, 0.5]$, $Pr = 0.786$, $\Gamma = 1$.

level would be chosen as the arithmetic mean temperature the later obtained BL thicknesses were closer to our results in the case of larger Ra.

6.2. *Boundary layer thickness*

Finally we compare the BL thicknesses for different Ra, starting with the thermal BL in figure 19(a), where the time averaged BL thickness along l_{LSC} is presented in units of $H/(2Nu)$. We observe a nearly linear and Ra-independent increase of this normalized thermal BL thickness along the wind, i.e. within J, for decreasing r. Since the p.d.f. of $\delta_T/(H/(2Nu))$ presented in figure 19(b) shows an almost Ra-independent behaviour the normalization with Nu compensates perfectly the decreasing BL thickness with growing Ra. Thus the p.d.f. found is universal (for the investigated triplets (Ra, Pr, Γ)) and the mean δ_T shows an Ra scaling

$$\langle \delta_T \rangle_{t,r} \sim 1/Nu \sim Ra^{-0.285 \pm 0.003}. \tag{6.1}$$

As one can see from figure 19(b), the BL thickness is distributed almost symmetrically around 85 % of its approximated value if a logarithmic scale is used.

In the case of the viscous BL the rescaling of the BL thickness with an approximated value is more complicated since no proper value exists. In figure 20(a) the p.d.f. of the viscous BL thickness δ_u reflects a Gaussian-like behaviour if scaled logarithmically. If the (not rescaled) p.d.f.s with logarithmic scale are fitted with a Gaussian curve, the most probable BL thickness δ_u^c can be evaluated. This δ_u^c shows a

https://doi.org/10.1017/jfm.2012.69 Published online by Cambridge University Press

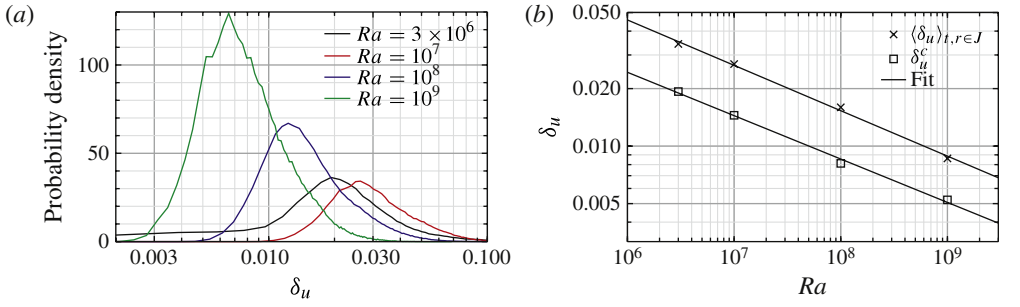


FIGURE 20. (*a*) p.d.f. of viscous boundary layer thickness δ_u for $r \in [-0.7, 0.5]$ and (*b*) fit of most probable δ_u versus Ra, $Pr = 0.786$, $\Gamma = 1$.

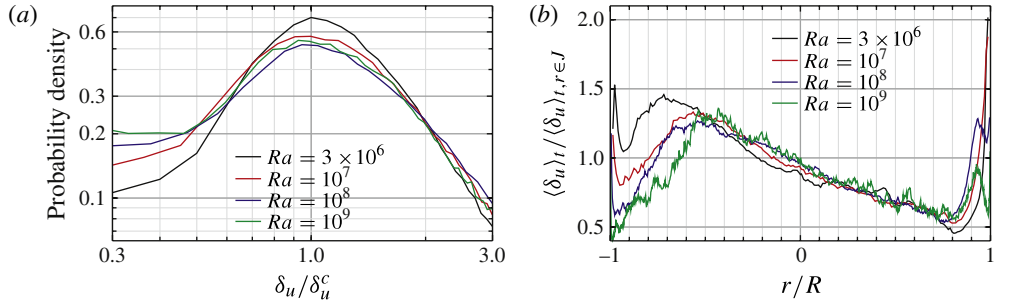


FIGURE 21. (*a*) p.d.f. of viscous boundary layer thickness δ_u scaled with the most probable value δ_u^c for $r \in [-0.7, 0.5]$ and (*b*) time-averaged viscous BL thickness in units of its mean value, $Pr = 0.786$, $\Gamma = 1$.

Ra-dependence (shown in figure 20*b*)

$$\delta_u^c \sim Ra^{-0.227\pm0.010}, \tag{6.2}$$

while $\langle \delta_u \rangle_{t,r\in J}$ scales as

$$\langle \delta_u \rangle_{t,r\in J} \sim Ra^{-0.238\pm0.009} \tag{6.3}$$

and is larger than δ_u^c as expected from the p.d.f.

Thus the exponent in the scaling of the viscous BL thickness with Ra is slightly smaller than that in the scaling of the thermal BL thickness, which lets us conclude that their ratio δ_T/δ_u is slightly decreasing with increasing Ra. Using the most probable value δ_u^c for the rescaling, we obtain a similar behaviour for all treated Ra (see figure 21*a*) as in the case of the thermal BL and as reported by Zhou & Xia (2010). Like in the case of δ_T the mean thickness of the viscous BL increases almost linearly along l_{LSC} (see figure 21*b*).

Besides the individual BL thicknesses also their ratio δ_T/δ_u is of interest. In figure 22 the mean ratio δ_T/δ_u over l_{LSC} and its p.d.f. are shown for different Ra. We observe that along the plate the ratio remains almost constant within J but slightly decreases with increasing Ra. This is exactly what is expected from the previous results. Indeed, the time averaged thermal and viscous BL thicknesses develop almost linearly along the plate, therefore their ratio was expected to be constant within J.

https://doi.org/10.1017/jfm.2012.69 Published online by Cambridge University Press

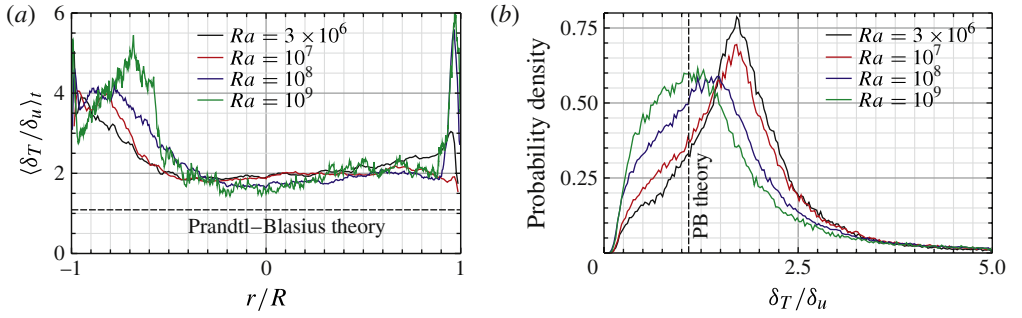


FIGURE 22. Ratio δ_T/δ_u, (*a*) time-averaged and (*b*) p.d.f. for $r \in [-0.7, 0.5]$, $Pr = 0.786$, $\Gamma = 1$. The dashed lines correspond to the prediction by Prandtl–Blasius (PB) theory (Shishkina *et al.* 2010).

Furthermore, as the individual BL thicknesses scale with Ra in a different way, an Ra-dependent ratio is obtained. The p.d.f.s in figure 22(*b*) reflect that there is a qualitative change from the lower to the higher Ra cases. This might by due to a change in the dynamics of the systems around $Ra = 10^8$ as was proposed in the theory by Grossmann & Lohse (2001) and supported by the Nu versus Ra dependence presented in figure 2.

7. Comparison with existing theories and models

In the present section the DNS results are first compared to classical BL theories with special focus on the spatial development of the BL thickness and the wind velocity. Further the scalings of integral quantities are compared to theoretical predictions based on different assumptions with respect to the BL theories.

7.1. *Boundary layer theories*

Since we have reduced our analysis to a two-dimensional situation with a wind along the flat bottom plate, the obtained results can be compared to the Prandtl–Blasius (PB) theory of laminar BLs (Schlichting & Gersten 2006). This theory is an approximation of the full governing equation (2.1) applied to the laminar flow parallel to a flat plate of semi-infinite length with a constant wind velocity and no temperature influence on the velocity field. Thus, beside the two-dimensionality several other assumptions are implied. There is first of all the geometry of the flat plate which of course differs from the geometry of a confined Rayleigh–Bénard cell. Studying the influence of the geometry on the development of the BL is far beyond the scope of this paper but it should be mentioned that even for large aspect ratios the large-scale structures have a finite size (Hartlep, Tilgner & Busse 2003; Bailon-Cuba *et al.* 2010). The next strong assumption in PB approach is that the temperature is treated as a passive scalar and has no influence on the velocity field. Even though a large effect of buoyancy is expected (due to the occurrence of thermal plumes) a deeper analysis must be left for future studies. In addition the laminarity of the flow is a necessary ingredient of the PB ansatz.

It is well-known that RBC becomes turbulent if a critical Ra is reached (Ahlers *et al.* 2009*b*), but this does not mean that there are dominant fluctuations in the BL region. To check this we use first of all a theoretical approach (Landau & Lifschitz 2007) for the occurrence of an increasing Tollmien–Schlichting instability within the BL close

https://doi.org/10.1017/jfm.2012.69 Published online by Cambridge University Press

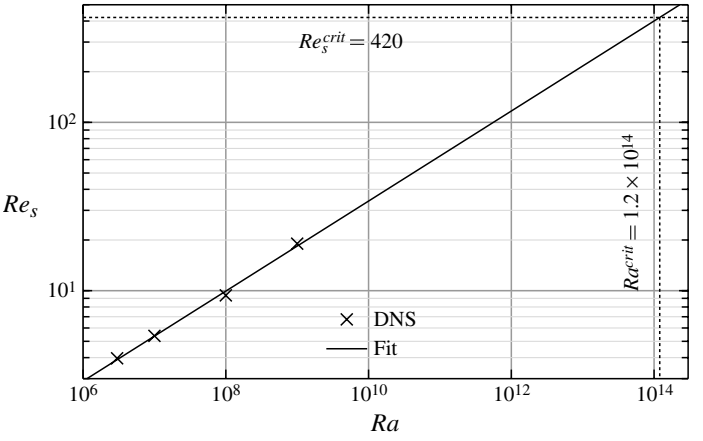


FIGURE 23. $Re_s = \Gamma^{3/2} Ra^{1/2} Pr^{-1/2} U \delta_u / 2$ versus Ra and critical Ra with respect to the Tollmien–Schlichting instability, $Pr = 0.786$, $\Gamma = 1$.

to a flat plate. The critical shear Reynolds number is estimated as $Re_s^{crit} \approx 420$ where $Re_s = \widehat{U}\widehat{\delta^*}/\widehat{\nu}$, $\widehat{U}$ is the (constant) wind velocity, $\widehat{\delta^*}$ is the displacement thickness and the hat again marks dimensional quantities. The displacement thickness is connected to our definition of the boundary layer thickness by $\delta^* \approx \delta_u/2$. This can be seen easily by the definition of the displacement thickness (Schlichting & Gersten 2006) applied to an assumed linear profile. Thus Re_s with our set of references reads $Re_s = \Gamma^{3/2} Ra^{1/2} Pr^{-1/2} U \delta_u / 2$. Of course, in the case of RBC the critical Re_s might be strongly influenced by the geometry and buoyancy but the above relation can be used to estimate the critical Re_s. We use the most probable viscous BL thickness δ_u^c and the largest mean velocity level $\max_{r \in J}(\langle u_L \rangle_t)$ and thus obtain the scaling (see figure 23)

$$Re_s = 0.072 \times Ra^{0.2675} \tag{7.1}$$

based on our DNS data. Extrapolation to higher Ra tells us therefore that for $Ra^{crit} = 1.2 \times 10^{14}$ the critical limit $Re_s = 420$ is reached. Because all the Ra covered in our DNS are more than five decades smaller than the critical one, we thus conclude that within this estimate our BLs are expected to be predominantly laminar. Note that Sun *et al.* (2008) found $Ra^{crit} = 2 \times 10^{13}$ for quasi-two-dimensional experiments in water.

Even though we are far below Ra^{crit}, we observe fluctuations in the BL region. We therefore calculate Reynolds stresses (Schlichting & Gersten 2006) and compare the contribution of the fluctuations (turbulent stress) with the total stress, i.e. the sum of the absolutes of laminar and turbulent stresses, and thus the functions

$$\chi_u(r,z) = \frac{\left|(u_r - \langle u_r \rangle_t)(u_z - \langle u_z \rangle_t)\right|}{Pr^{1/2}\Gamma^{-3/2}Ra^{-1/2}\left|\partial_z u_r\right| + \left|(u_r - \langle u_r \rangle_t)(u_z - \langle u_z \rangle_t)\right|}, \tag{7.2}$$

$$\chi_T(r,z) = \frac{\left|(T - \langle T \rangle_t)(u_z - \langle u_z \rangle_t)\right|}{Pr^{-1/2}\Gamma^{-3/2}Ra^{-1/2}\left|\partial_z T\right| + \left|(T - \langle T \rangle_t)(u_z - \langle u_z \rangle_t)\right|} \tag{7.3}$$

for the region close to the wall within the LSC plane. Their values vary between zero and one. These limit values correspond to vanishing or infinitely large fluctuations,

https://doi.org/10.1017/jfm.2012.69 Published online by Cambridge University Press

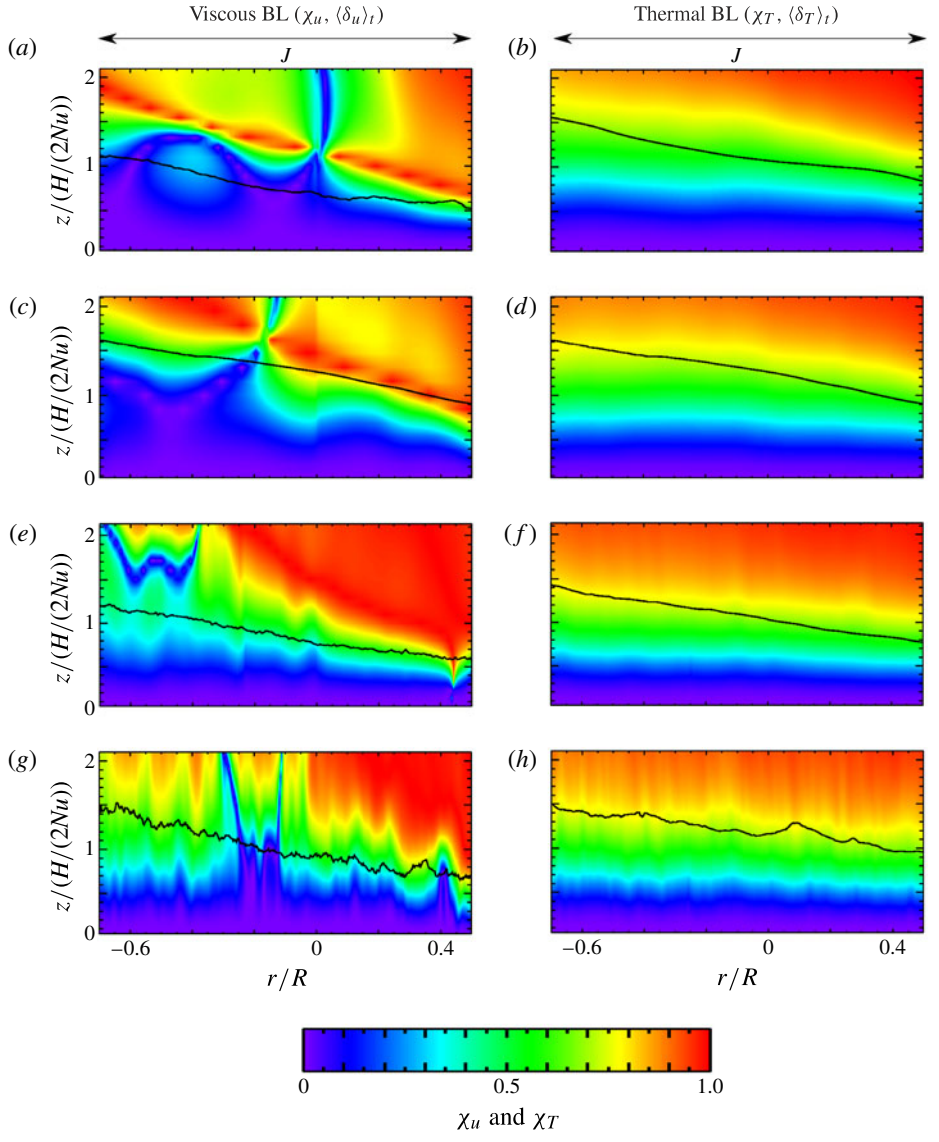


FIGURE 24. Relative contributions of fluctuations in the BL region expressed by Reynolds stresses for the viscous (χ_u) (*a,c,e,g*) and thermal (χ_T) (*b,d,f,h*) BL (see (7.2), (7.3)). Colour: (*a*) χ_u for $Ra = 3 \times 10^6$, (*b*) χ_T for $Ra = 3 \times 10^6$, (*c*) χ_u for $Ra = 10^7$, (*d*) χ_T for $Ra = 10^7$, (*e*) χ_u for $Ra = 10^8$, (*f*) χ_T for $Ra = 10^8$, (*g*) χ_u for $Ra = 10^9$, (*h*) χ_T for $Ra = 10^9$, black lines: corresponding mean thicknesses of viscous and thermal BL, $Pr = 0.786$, $\Gamma = 1$.

respectively. We therefore imply a two-dimensional flow with spatially constant mean wind along a plate and thus neglect fluctuations perpendicular to the LSC plane and buoyancy.

The resulting functions χ_u and χ_T are presented in figure 24 in colour together with the mean thicknesses of the viscous BL (case of χ_u) and the thermal BL (case of χ_T) for different Ra. First of all it is observed that χ_u and χ_T behave in completely different ways and second that the functions depend weakly on Ra. Close

https://doi.org/10.1017/jfm.2012.69 Published online by Cambridge University Press

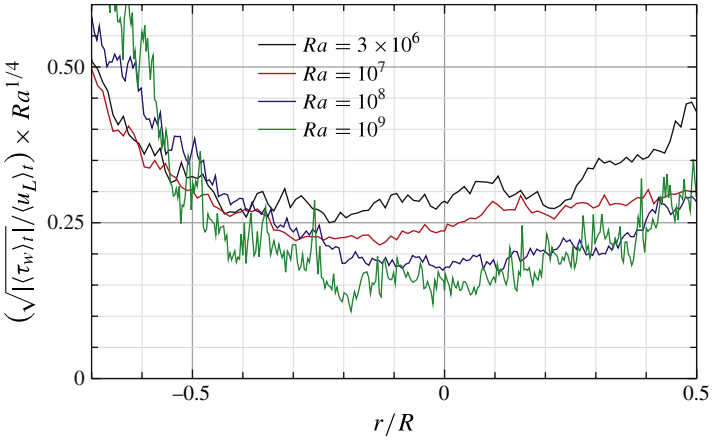


FIGURE 25. Ratio $\sqrt{|\langle\tau_w\rangle_t|}/|\langle u_L\rangle_t|$ (rescaled for clarity with $Ra^{1/4}$) for different Ra, $Pr = 0.786$, $\Gamma = 1$.

to the bottom plate the fluctuations are suppressed and the stress is thus dominated by the gradient of wind velocity/temperature. For larger distances from the wall the fluctuations grow and lead to higher χ. At the heights of the mean BL thicknesses χ_u and χ_T grow to 0.5–0.7, which means that the fluctuating contribution is of the same size or even slightly larger than the gradient contribution. Therefore especially for the thermal BL the assumption of negligible fluctuations is questionable. This implies that for moderate and large Ra the influence of these fluctuations, which are not part of the PB theory cannot be neglected and should be investigated in more detail in the future.

Further we observed that the thicknesses of the thermal and the viscous BL increase almost linearly in the direction of the wind as it was already shown in figures 19(*a*) and 21(*b*). Contrary to this PB theory predicts an increase with the square root of the distance along the plate (Schlichting & Gersten 2006). In fact an almost linear increase is typical for a turbulent BL developing along a flat plate (Landau & Lifschitz 2007) under the assumption of a constant mean wind velocity. But the linear increase is not a sufficient criterion for a turbulent BL. One of the additional requirements is the validity of

$$\frac{\mathrm{d}\langle\delta_u\rangle_t}{\mathrm{d}x} \sim \frac{\sqrt{|\langle\tau_w\rangle_t|}}{|\langle u_L\rangle_t|}, \tag{7.4}$$

where x is the wind direction (here radial). It follows directly from an order of magnitude analysis (Landau & Lifschitz 2007). The right-hand side of (7.4) is evaluated in figure 25 and expected to be constant, since the BL thickness is increasing linearly. This is not observed, especially for larger Ra for which the effects of turbulence should be stronger.

Besides this the BL profiles in the case of a turbulent BL must contain a logarithmic behaviour as was obtained by Hölling & Herwig (2006). On the other hand recent studies by Zhou & Xia (2010) show that PB profiles can be obtained if a proper rearranging is performed. To clarify these conflicting results we consider time-averaged local profiles for $Ra = 10^9$ at $r = -0.1$. This choice is motivated by the fact that we expect the strongest influence of fluctuations for our highest Ra while the position corresponds to the maximal wind magnitude. In figure 26 the time averaged

https://doi.org/10.1017/jfm.2012.69 Published online by Cambridge University Press

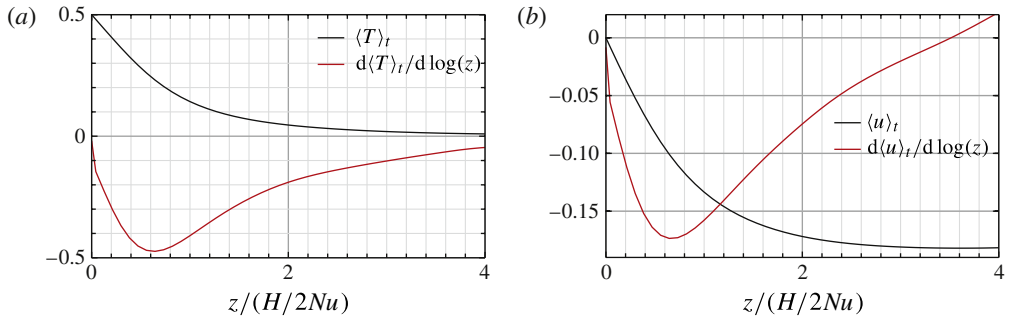


FIGURE 26. Local profiles at $r = -0.1$ of (a) the temperature and (b) the wind velocity in combination with diagnostic functions indicating the occurrence of a logarithmic behaviour if a plateau is present for $Ra = 10^9$, $Pr = 0.786$, $\Gamma = 1$.

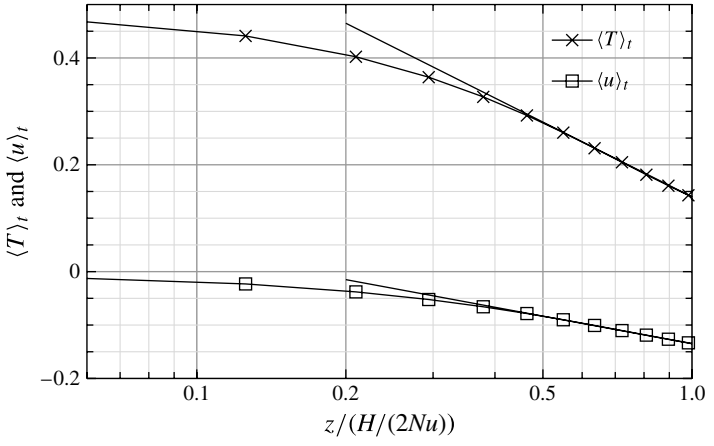


FIGURE 27. Local profiles at $r = -0.1$ of the temperature and the wind velocity with logarithmic spatial scale, $Ra = 10^9$, $Pr = 0.786$, $\Gamma = 1$.

temperature (a) and velocity (b) profiles are shown for this position. In addition diagnostic functions for the occurrence of a logarithmic behaviour are given (see Shishkina & Thess 2009). A plateau of $\mathrm{d}f(z)/\mathrm{d}\log(z)$ indicates thereby the presence of a logarithmic behaviour. Apparently no plateau is obtained but for both profiles an extremum below $H/2Nu$ is visible. Figure 27 provides another less quantitative presentation of the profiles depicted with a logarithmic length scale. The figure reveals an almost linear behaviour within the upper two-thirds of the BL, which is equivalent to a logarithmic behaviour on a linear scale. Thus we want to emphasize that although in a logarithmic scale the profiles almost coincide with straight lines (figure 27) in a certain region, they are essentially non-logarithmic as illustrated by the diagnostic functions in figure 26. This together with the invalidity of (7.4) suggests that the linear increase of the BL thicknesses is not simply caused by turbulent BLs.

Another interesting quantity is the ratio of the BL thicknesses δ_T/δ_u, since according to PB theory it can be approximated by an Ra-independent (constant) value (Shishkina *et al.* 2010). As previously shown the thermal BL thickness can be approximated using Nu and thus knowledge of the ratio allows to approximate the viscous BL thickness.

https://doi.org/10.1017/jfm.2012.69 Published online by Cambridge University Press

Our results imply that the ratio is almost constant in the direction of the wind and approaches its theoretical value with increasing Ra (see figure 22). This can also be seen from the Ra-scaling of the BL thicknesses shown in the previous section. From this we obtain the ratio scaling $\delta_T/\delta_u \sim Ra^{-0.05}$ (which is of course only an approximation because of neglected correlations). Still, for the considered range of Ra the theoretical value $\delta_T/\delta_u = Pr^{-0.357+0.022\log_{10}(Pr)} = 1.09$ (Shishkina *et al.* 2010) is almost reached. Similarly the p.d.f.s in figure 22(*b*) reveal that the theoretical values are approached for higher Ra. This result is quite surprising since on the one hand the ratio follows the prediction of PB theory to be spatially constant, on the other hand depends on Ra which is in contradiction to PB theory. Furthermore the Ra-dependence leads to better agreement with the PB theory for higher Ra, for which larger effects of the fluctuations are expected. Stevens, Lohse & Verzicco (2011*b*) also found a reasonable agreement with PB theory. They obtained about 15 % smaller values δ_T/δ_u compared to ours. A possible reason for this discrepancy is that Stevens *et al.* (2011*b*) determine δ_u in a different way: they use the point of maximum of the quantity $\boldsymbol{u}\cdot\nabla^2\boldsymbol{u}$ in the vicinity of the wall instead of the slope criterion.

Besides the fluctuations another BL characteristic might lead to deviations from the classical BL theories. To our knowledge in all discussed models the assumption of a *constant wind* along the plate is made. In figure 17(*a*) we have shown that the wind is varying strongly along the plate (as also shown by Zhou *et al.* (2011) in two-dimensional DNS) and the horizontal component of the mean wind velocity even vanishes at some points. Therefore a further investigation of the influence of such a spatially varying wind on the BL characteristics is needed. We leave this point open for future studies.

7.2. *Scaling of integral quantities*

Besides the comparison with PB theory in a direct way we compare integral quantities derived from the DNS data with predictions of Grossmann–Lohse (GL) theory (Grossmann & Lohse 2000; Ahlers *et al.* 2009*b*) partly based on PB BLs, and the theories by Shraiman & Siggia (1990) and Hölling & Herwig (2006) which consider turbulent BLs. First of all the Reynolds number Re obtained is compared to the theories in two different ways. On the one hand it is possible to calculate Re using the wall shear stress obtained along l_{LSC} (see figure 12*a*). If we consider the maximal absolute dimensionless wall shear stress τ_w^{max} within the r-interval J, we find $\tau_w^{max} \sim Ra^{\gamma}$ with $\gamma = 0.221$. In contrast, if we consider the mean wall shear stress $\langle\tau_w\rangle_r$ within J, we obtain $\langle\tau_w\rangle_r \sim Ra^{\gamma}$ with $\gamma = 0.206$ (see figure 28). The scalings are of course correct only if the above-mentioned set of reference quantities is used. To simplify the comparison we therefore recall dimensional quantities at this point (and again mark them with a hat). Since for the reference velocity $u_{ref} \sim Ra^{1/2}$, we obtain $\hat{\tau}_w \sim Ra^{\gamma+1/2}$. From PB theory we obtain that $Re \sim \hat{\tau}_w^{2/3}$ (Shishkina *et al.* 2010). Applying the scaling of $\widehat{\tau_w}$ with Ra, obtained in the DNS, gives us

$$Re \sim \hat{\tau}_w^{2/3} \sim (Ra^{\gamma+1/2})^{2/3} = Ra^{(2\gamma+1)/3} = \begin{cases} Ra^{0.481} & \text{for } \tau_w^{max}, \\ Ra^{0.471} & \text{for } \langle\tau_w\rangle_r. \end{cases} \tag{7.5}$$

GL theory predicts the scaling depending on different regimes within (Ra, Pr)-space, in particular for regime II_l $Re \sim Ra^{2/5}$ and for regime IV_l $Re \sim Ra^{1/2}$, where most of the treated pairs (Ra, Pr) are within IV_l and for smaller Ra they are in II_l. Therefore we find a good agreement.

https://doi.org/10.1017/jfm.2012.69 Published online by Cambridge University Press

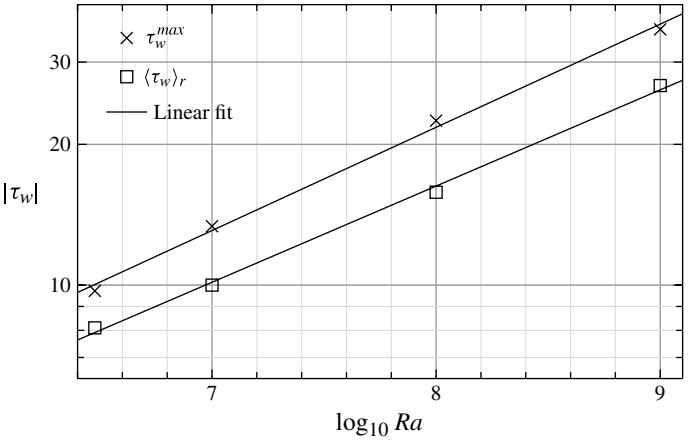


FIGURE 28. *Re* versus *Ra* scaling obtained from the wall shear stress by using PB theory, $Pr = 0.786$, $\Gamma = 1$.

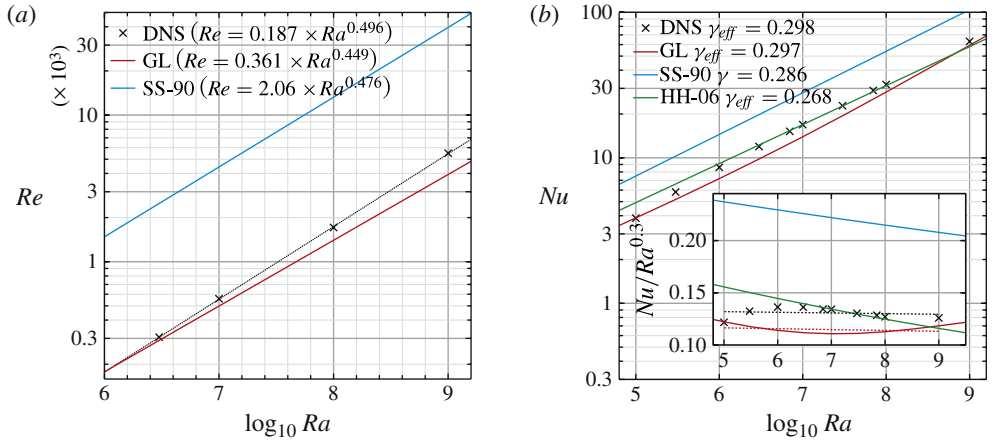


FIGURE 29. Scalings from our DNS in comparison with existing theories. (*a*) *Re* versus *Ra* scaling and (*b*) *Nu* versus *Ra* scaling in comparison with predictions from the theory by Grossmann & Lohse (2000) (GL), the theory by Shraiman & Siggia (1990) (SS-90) and the theory by Hölling & Herwig (2006) (HH-06). Inset of (*b*): reduced *Nu* versus *Ra* and fitting to obtain effective scaling exponents γ_{eff}, $Pr = 0.786$, $\Gamma = 1$.

The velocity levels obtained for different *Ra* can be used to compare the *Re* versus *Ra* scaling with the theories in a more quantitative way. We calculate *Re* by means of the height of the cell *H*, the mean velocity level $U = \langle u_L \rangle_{t,r\in J}$ and the (constant) viscosity which reads in our units $Re = \Gamma^{3/2} Ra^{1/2} Pr^{-1/2} UH$. By linear fitting *Re* versus *Ra* the scaling

$$Re = 0.187 \times Ra^{0.496} \tag{7.6}$$

https://doi.org/10.1017/jfm.2012.69 Published online by Cambridge University Press

is obtained. The results are shown in figure 29(*a*) in comparison with predictions from GL theory for the corresponding regimes and with the theory by Shraiman & Siggia (1990).

Here for the theory of Grossmann & Lohse (2001) no single regimes have been considered but the set of coupled equations

$$NuRaPr^{-2} = c_1 Re^2 g\left(\sqrt{Re_c/Re}\right)^{-1} + c_2 Re^3, \tag{7.7}$$

$$Nu = c_3 Re^{1/2} Pr^{1/2} f\left(2aNuRe_c^{-1/2} g\left(\sqrt{Re_c/Re}\right)\right)^{1/2} + c_4 PrRef\left(2aNuRe_c^{-1/2} g\left(\sqrt{Re_c/Re}\right)\right), \tag{7.8}$$

with $f(x) = (1+x^4)^{-1/4}$, $g(x) = x(1+x^4)^{-1/4}$, $a = 0.482$, $c_1 = 8.685$, $c_2 = 1.441$, $c_3 = 0.462$, $c_4 = 0.013$ and $Re_c = 1.041$ has been solved numerically for Re and Nu. Then a linear fitting has been performed to obtain effective scalings for the considered Ra range. The scaling laws are given in figure 29(*a*). In all cases scaling exponents slightly below $1/2$ are obtained while the prefactor varies strongly. This might be due to the choice of the reference velocity which is somewhat arbitrary. In the literature different velocities are used which show similar scalings while their absolute values vary (Ahlers *et al.* 2009*b*).

Easier is the comparison for Nu as the absolute value is not influenced by the choice. As reported in § 3 the DNS results are in good agreement with experiments with respect to Nu. Here, the main focus should be on comparison with three theories based on different assumptions. Besides the GL theory the theories by Shraiman & Siggia (1990) (SS-90) and Hölling & Herwig (2006) (HH-06) should be considered. Neither theory includes different regimes as the GL theory does. While HH-06 considers the fully turbulent BLs (as they obtained in DNS and experiments in a way similar to figure 27), SS-90 predicts turbulent viscous and laminar thermal BLs. The latter is justified by a thermal BL nesting in the viscous one. As shown before, the thermal BL is always thicker than the viscous one for our Ra, Pr, Γ combination, therefore this assumption seems to be questionable in our case. Shraiman & Siggia (1990) predict the validity of their theory for the considered Pr within $3 \times 10^7 \lesssim Ra \lesssim 10^{13}$.

In figure 29(*b*) a comparison of our DNS data with the three theories is provided. Of course, none of the theories reproduces the DNS results over the whole considered Ra range exactly. For a small Ra interval $10^7 \lesssim Ra \lesssim 10^8$ there is a quite good agreement with Hölling & Herwig (2006). The effective scaling exponent γ_{eff} in the theory by Grossmann & Lohse (2001), determined with a linear fit within the complete considered Ra-interval, is found to agree best with the exponent obtained from our DNS results. Furthermore, only this theory predicts increasing scaling exponents for $Ra \gtrsim 10^8$ in agreement with the experimental and numerical results presented in figure 2.

8. Conclusions

Direct numerical simulations of Rayleigh–Bénard convection in a cylindrical container with aspect ratio one for $Pr = 0.786$ and $Ra = 10^4$–10^9 have been performed in order to analyse the boundary layers thickness and related quantities. The analysis is restricted to the plane of the large-scale circulation and in particular the viscous and thermal boundary layers in the region close to the bottom plate. Methods to support this analysis are presented and discussed in detail. This includes time averaging over periods without major reorientations and a local and instantaneous determination of the

https://doi.org/10.1017/jfm.2012.69 Published online by Cambridge University Press

boundary layer thicknesses and the wind velocity. Therefore not only mean values but also probability density functions are analysed.

The results can be summarized as follows: the time-averaged boundary layer thicknesses show a linear increase along the wind direction which occurs for all *Ra* considered,while their ratio stays spatially constant and converges slowly with growing *Ra* against its theoretical prediction based on Prandtl–Blasius theory. The linear increase of the boundary layer thicknesses is a deviation from Prandtl–Blasius theory and might be explained by domination of fluctuations in the boundary layer region. Nevertheless the evaluation of the diagnostic functions for the presence of the logarithmical BL profiles has not confirmed the presence of fully turbulent BLs for the Rayleigh numbers considered either. In contrast the presence of a spatially varying wind magnitude which is partly dictated by the confined geometry of the convection cell, might be one reason for the linear increase of the BL thickness. This fact is independent of whether fluctuations in the boundary layer region are accounted for. To our knowledge, all boundary layer models considered in the theory of RBC have neglected this fact so far. Nevertheless, the integral quantities *Nu* and *Re* can be predicted well based on the assumptions of a constant wind.

Acknowledgements

The authors would like to thank G. Ahlers and J. Schumacher for fruitful discussions and helpful comments. Furthermore they are grateful to S. Horn for updating the DNS code (Horn, Shishkina & Wagner 2011) and providing several postprocessing routines and acknowledge support by the Deutsche Forschungsgemeinschaft (DFG) under grant SH405/2-1.

REFERENCES

AHLERS, G., BODENSCHATZ, E., FUNFSCHILLING, D. & HOGG, J. 2009*a* Turbulent Rayleigh–Bénard convection for a Prandtl number of 0.67. *J. Fluid Mech.* **641**, 157–167.

AHLERS, G., GROSSMANN, S. & LOHSE, D. 2009*b* Heat transfer and large-scale dynamics in turbulent Rayleigh–Bénard convection. *Rev. Mod. Phys.* **82**, 503–537.

BAILON-CUBA, J., EMRAN, M. S. & SCHUMACHER, J. 2010 Aspect ratio dependence of heat transfer and large-scale flow in turbulent convection. *J. Fluid Mech.* **655**, 152–173.

BROWN, E. & AHLERS, G. 2006 Rotations and cessations of the large-scale circulation in turbulent Rayleigh–Bénard convection. *J. Fluid Mech.* **568**, 351–386.

BROWN, E. & AHLERS, G. 2009 The origin of oscillations of the large-scale circulation of turbulent Rayleigh–Bénard convection. *J. Fluid Mech.* **638**, 383–400.

CASTAING, B., GUNARATNE, G., HESLOT, F., KADANOFF, L., LIBCHABER, A., THOMAE, S., WU, X.-Z., ZALESKI, S. & ZANETTI, G. 1989 Scaling of hard thermal turbulence in Rayleigh–Bénard convection. *J. Fluid Mech.* **204**, 1–30.

CHAVANNE, X., CHILLÀ, F., CHABAUD, B., CASTAING, B. & HÉBRAL, B. 2001 Turbulent Rayleigh–Bénard convection in gaseous and liquid He. *Phys. Fluids* **13**, 1300–1320.

CIONI, S., CILIBERTO, S. & SOMMERIA, J. 1997 Strongly turbulent Rayleigh–Bénard convection in mercury: comparison with results at moderate Prandtl number. *J. Fluid Mech.* **335**, 111–140.

FUNFSCHILLING, D. & AHLERS, G. 2004 Plume motion and large-scale dynamics in a cylindrical Rayleigh–Bénard cell. *Phys. Rev. Lett.* **92**, 194502.

FUNFSCHILLING, D., BROWN, E. & AHLERS, G. 2008 Torsional oscillations of the large-scale circulation in turbulent Rayleigh–Bénard convection. *J. Fluid Mech.* **607**, 119–139.

GROSSMANN, S. & LOHSE, D. 2000 Scaling in thermal convection: A unifying view. *J. Fluid Mech.* **407**, 27–56.

GROSSMANN, S. & LOHSE, D. 2001 Thermal convection for large Prandtl number. *Phys. Rev. Lett.* **86**, 3316–3319.

https://doi.org/10.1017/jfm.2012.69 Published online by Cambridge University Press

GROSSMANN, S. & LOHSE, D. 2011 Multiple scaling in the ultimate regime of thermal convection. *Phys. Fluids* **23**, 045108.

HARTLEP, T., TILGNER, A. & BUSSE, F. H. 2003 Large scale structures in Rayleigh–Bénard convection at high Rayleigh numbers. *Phys. Rev. Lett.* **91**, 064501.

HÖLLING, M. & HERWIG, H. 2006 Asymptotic analysis of heat transfer in turbulent Rayleigh–Bénard convection. *Intl J. Heat Mass Transfer* **49**, 1129–1136.

HORN, S., SHISHKINA, O. & WAGNER, C. 2011 The influence of non-Oberbeck–Boussinesq effects on rotating turbulent Rayleigh–Bénard convection. *J. Phys.: Conf. Ser.* **318**, 082005.

KACZOROWSKI, M., SHISHKINA, O., SHISHKIN, A., WAGNER, C. & XIA, K.-Q. 2011 Analysis of the large-scale circulation and the boundary layers in turbulent Rayleigh–Bénard convection. In *Direct and Large-Eddy Simulation VIII* (ed. H. Kuerten, B. Geurts, V. Armenio & J. Fröhlich), pp. 383–388. Springer.

KRAICHNAN, R. 1962 Turbulent thermal convection at arbitrary Prandtl number. *Phys. Fluids* **5**, 1374–1389.

KUNNEN, R. P. J., CLERCX, H. J. H., GEURTS, B. J., BOKHOVEN, L. J. A. V., AKKERMANS, R. A. D. & VERZICCO, R. 2008 Numerical and experimental investigation of structure-function scaling in turbulent Rayleigh–Bénard convection. *Phys. Rev.* E **77**, 016302.

LANDAU, L. D. & LIFSCHITZ, E. M. 2007 Hydrodynamik. In *Lehrbuch der theoretischen Physik,* vol. 6, 5th edn. Harri Deutsch.

LOHSE, D. & XIA, K.-Q. 2010 Small-scale properties of turbulent Rayleigh–Bénard convection. *Annu. Rev. Fluid Mech.* **42**, 335–364.

MISHRA, P. K., DE, A. K., VERMA, M. K. & ESWARAN, V. 2011 Dynamics of re-orientations and reversals of large-scale flow in Rayleigh–Bénard convection. *J. Fluid Mech.* **668**, 480–499.

NIEMELA, J. J. & SREENIVASAN, K. R. 2003 Confined turbulent convection. *J. Fluid Mech.* **481**, 355–384.

DU PUITS, R., RESAGK, C. & THESS, A. 2009 Structure of viscous boundary layers in turbulent Rayleigh–Bénard convection. *Phys. Rev.* E **80**, 036318.

RESAGK, C., DU PUITS, R., THESS, A., DALZHANSKY, F. V., GROSSMANN, S., ARAUJO, F. F. & LOHSE, D. 2006 Oszillations of the large-scale wind in turbulent thermal convection. *Phys. Fluids* **18**, 095105.

ROCHE, P.-E., CASTAING, B., CHABAUD, B. & HÉBRAL, B. 2003 Heat transfer in turbulent Rayleigh–Bénard convection below the ultimate regime. *J. Low Temp. Phys.* **134**, 1011–1042.

SCHLICHTING, H. & GERSTEN, K. 2006 *Grenzschicht-Theorie*, 10th edn. Springer.

SCHMALZL, J., BREUER, M. & HANSEN, U. 2004 On the validity of two-dimensional numerical approaches to time-dependend thermal convection. *Europhys. Lett.* **67**, 390–396.

SCHMITT, L., RICHTER, K. & FRIEDRICH, R. 1986 Large-eddy simulation of turbulent boundary layer and channel flow at high Reynolds number. In *Direct and Large Eddy Simulation of Turbulence* (ed. U. Schumann & R. Friedrich). pp. 161–176. Vieweg.

SCHUMANN, U. 1973 Ein Verfahren zur direkten numerischen Simulation turbulenter Strömungen in Platten- und Ringspaltkanälen und über seine Anwendung zur Untersuchung von Turbulenzmodellen. PhD thesis, TH Karlsruhe, KFK 1854.

SHISHKINA, O., STEVENS, R. J. A. M., GROSSMANN, S. & LOHSE, D. 2010 Boundary layer structure in turbulent thermal convection and its consequences for the required numerical resolution. *New J. Phys.* **12**, 075022.

SHISHKINA, O. & THESS, A. 2009 Mean temperature profiles in turbulent Rayleigh–Bénard convection of water. *J. Fluid Mech.* **663**, 449–460.

SHISHKINA, O. & WAGNER, C. 2005 A fourth-order accurate finite volume scheme for numerical simulations of turbulent Rayleigh–Bénard convection in cylindrical containers. *C. R. Mecanique* **333**, 17–28.

SHISHKINA, O. & WAGNER, C. 2007 Local heat fluxes in turbulent Rayleigh–Bénard convection. *Phys. Fluids* **19**, 085107.

SHRAIMAN, B. & SIGGIA, E. 1990 Heat transport in high-Rayleigh-number convection. *Phys. Rev.* A **42**, 3650–3653.

https://doi.org/10.1017/jfm.2012.69 Published online by Cambridge University Press

STEVENS, R. J. A. M., CLERCX, H. J. H. & LOHSE, D. 2011*a* Effect of plumes on measuring the large-scale circulation in turbulent Rayleigh–Bénard convection. *Phys. Fluids* **23**, 095110.

STEVENS, R. J. A. M., LOHSE, D. & VERZICCO, R. 2011*b* Prandtl and Rayleigh number dependence of heat transport in heigh Rayleigh number thermal convection. *J. Fluid Mech.* **688**, 31–43.

STEVENS, R. J. A. M., VERZICCO, R. & LOHSE, D. 2010 Radial boundary layer structure and Nusselt number in turbulent Rayleigh–Bénard convection. *J. Fluid Mech.* **643**, 495–507.

SUGIYAMA, K., NI, R., STEVENS, R. J. A. M., CHAN, T. S., ZHOU, S.-Q., XI, H.-D., SUN, C., GROSSMANN, S., XIA, K.-Q. & LOHSE, D. 2010 Flow reversals in thermally driven turbulence. *Phys. Rev. Lett.* **105**, 034503.

SUN, C., CHEUNG, Y.-H. & XIA, K.-Q. 2008 Experimental studies of the viscous boundary layer properties in turbulent Rayleigh–Bénard convection. *J. Fluid Mech.* **605**, 79–113.

SUN, C., XIA, K.-Q. & TONG, P. 2005 Three-dimensional flow structures and dynamics of turbulent thermal convection in a cylindrical cell. *Phys. Rev.* E **72**, 026302.

TILGNER, A., BELMONTE, A. & LIBCHABER, A. 1993 Temperature and velocity profiles of turbulent convection in water. *Phys. Rev.* E **47**, 2253–2257.

XI, H.-D., ZHOU, Q. & XIA, K.-Q. 2006 Azimuthal motion of the mean wind in turbulent thermal convection. *Phys. Rev.* E **73**, 056312.

XI, H.-D., ZHOU, S.-Q., ZHOU, Q., CHAN, T. S. & XIA, K.-Q. 2009 Origin of the temperature oscillations in turbulent thermal convection. *Phys. Rev. Lett.* **102**, 044503.

XIA, K.-Q., SUN, C. & ZHOU, S. 2003 Particle image velocimetry measurement of the velocity field in turbulent thermal convection. *Phys. Rev.* E **68**, 066303.

ZHOU, Q., STEVENS, R. J. A. M., SUGIYAMA, K., GROSSMANN, S., LOHSE, D. & XIA, K.-Q. 2010 Prandtl–Blasius temperature and velocity boundary-layer profiles in turbulent Rayleigh–Bénard convection. *J. Fluid Mech.* **664**, 297–312.

ZHOU, Q., SUGIYAMA, K., STEVENS, R. J. A. M., GROSSMANN, S., LOHSE, D. & XIA, K.-Q. 2011 Horizontal structures of velocity and temperature boundary-layers in two-dimensional numerical turbulent Rayleigh–Bénard convection. *Phys. Fluids* **23**, 125104.

ZHOU, Q., XI, H.-D., ZHOU, S.-Q., SUN, C. & XIA, K.-Q. 2009 Oscillations of the large-scale circulation in turbulent Rayleigh–Bénard convection: the sloshing mode and its relationship with the torsional mode. *J. Fluid Mech.* **630**, 367–390.

ZHOU, Q. & XIA, K.-Q. 2010 Measured instantaneous viscous boundary layer in turbulent Rayleigh–Bénard convection. *Phys. Rev. Lett.* **104**, 104301.

https://doi.org/10.1017/jfm.2012.69 Published online by Cambridge University Press